The importance of free infragravity waves in the North Sea
Insights from field observations and unstructured SWAN modelling

Akrish, Gal; Reniers, Ad; Rijnsdorp, Dirk; Zijlema, Marcel; Rutten, Jantien; Tissier, Marion

DOI
10.1016/j.ocemod.2025.102619

Publication date
2025

Document Version
Final published version

Published in
Ocean Modelling

Citation (APA)
Akrish, G., Reniers, A., Rijnsdorp, D., Zijlema, M., Rutten, J., & Tissier, M. (2025). The importance of free infragravity waves in the North Sea: Insights from field observations and unstructured SWAN modelling. *Ocean Modelling*, *198*, Article 102619. https://doi.org/10.1016/j.ocemod.2025.102619

Ocean Modelling 198 (2025) 102619

Contents lists available at ScienceDirect

Ocean Modelling

journal homepage: www.elsevier.com/locate/ocemod

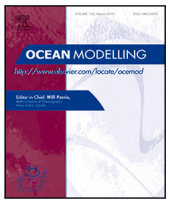

The importance of free infragravity waves in the North Sea: Insights from field observations and unstructured SWAN modelling

Gal Akrish [a,b,*], Ad Reniers [a], Dirk Rijnsdorp [c], Marcel Zijlema [a], Jantien Rutten [d], Marion Tissier [a]

[a] Department of Hydraulic Engineering, Faculty of Civil Engineering and Geosciences, Delft University of Technology, The Netherlands
[b] School of Mechanical Engineering, Faculty of Engineering, Tel Aviv University, Israel
[c] Siemens Gamesa Renewable Energy, 2595 BN The Hague, The Netherlands
[d] Unit of Hydraulic Engineering, Deltares, 2629 HV Delft, The Netherlands

ARTICLE INFO

Dataset link: Mean sea level bathymetry (Reference data), Measurement data (Reference data), Data collected at station REF (Reference data), Sea-swell data (Reference data), ERA5 hourly wind data (Reference data)

Keywords:
Infragravity waves
SWAN
Unstructured wave modelling
Infragravity wave observations
Nearshore wave conditions

ABSTRACT

This study examines the importance of free infragravity (FIG) waves in the North Sea using a recent collection of wave measurements and a newly developed unstructured SWAN model. The measurements include new observations of infragravity waves at offshore (30–40 m water depth) and nearshore (10–20 m water depth) locations in the southern North Sea. These observations serve as the basis for model optimization and verification. Good agreement is obtained between model predictions and measurements during two recent storm periods, including severe storms with unusual wind directions and high wind speeds (e.g., "Storm Babet"). Model investigation along the coasts of Belgium and the Netherlands demonstrated a strong dependence between nearshore FIG conditions (i.e., energy intensity and sources) and storm characteristics (i.e., alongshore wind pattern and storm track). Specifically, several storms have demonstrated significant contributions of FIG energy originating from remote sources (e.g., the coasts of UK and Denmark). This suggests that nearshore FIG conditions in the North Sea cannot be determined based on the local sea-swell conditions alone and may be significantly underestimated if non-local contributions are ignored. Finally, modelled and measured results at nearshore locations along the Dutch coast revealed that under storm conditions FIG energy can be an order of magnitude higher than energy due to bound infragravity (BIG) waves. This result, augmented with estimated ratios of free and forced infragravity energy at the shoreline, emphasizes the necessity of considering the FIG waves as an integral part of coastal safety assessments along the coasts of the North Sea.

1. Introduction

Infragravity (IG) waves are long waves which can significantly modulate storm surge and tide levels along the coasts around the globe (e.g., Dodet et al., 2019). In contrast to sea-swell waves, which are dissipating considerably nearshore due to breaking, the small steepness of IG waves allows them to penetrate deep into the surf-zone with minimal dissipation. Consequently, IG waves may be the dominant oscillating components during extreme sea levels (e.g., Guza and Thornton, 1982), leading to significant runup (e.g., Ruggiero et al., 2004) and overtopping (e.g., Cheriton et al., 2016) events and to considerable beach erosion and dune overwash (e.g., McCall et al., 2010). Following evidence collected during storms of the impacts associated with IG waves (e.g., Roeber and Bricker, 2015; Baumann et al., 2017), awareness of the need to include them as an integral part of coastal safety assessments has increased (e.g., Winter et al., 2020). Especially, due to the simultaneous increase in low-lying coastal population (e.g., Neumann et al., 2015) and in the frequency and intensity of coastal storms (e.g., Emanuel, 2013), the necessity to take the IG band into account for the development of coastal resilience strategies and early warning systems is becoming increasingly urgent.

State-of-the-art forecast systems of coastal flooding and erosion that include the impact of IG waves are based on coupling of large and small scale modelling approaches (e.g., Vousdoukas et al., 2012; Barnard et al., 2014; Turner et al., 2024). Large-scale models resolve the development of sea-swell waves, upper ocean circulation and atmospheric components (e.g., tides, surface currents, storm surges) which are then used as boundary conditions for small-scale nearshore models. The latter modelling approach is commonly based on high-resolution models which can predict the complicated processes characterize the swash-zone hydrodynamics (e.g., Roelvink et al., 2009; Zijlema et al., 2011). Within these forecast systems, the contribution of IG waves is introduced along the offshore boundaries of the small-scale models (usually defined along water depths of O(10 m)), estimated as the

* Corresponding author at: Department of Hydraulic Engineering, Faculty of Civil Engineering and Geosciences, Delft University of Technology, The Netherlands.
E-mail address: G.Akrish@tudelft.nl (G. Akrish).

https://doi.org/10.1016/j.ocemod.2025.102619
Received 19 April 2025; Received in revised form 7 August 2025; Accepted 7 August 2025
Available online 25 August 2025

second-order bound (phase-coupled) response to the local incident wind wave forcing (Hasselmann, 1962). Namely, current modelling practice assumes that shoreward propagation of IG waves nearshore are solely composed of bound IG (BIG) components. This assumption introduces uncertainty regarding the impact of IG waves, specifically because of the unknown presence of freely propagating IG (FIG) waves. The questions that arise in this context concern the relative importance of FIG compared to BIG waves at the offshore boundaries and the propagation of wave uncertainty from the offshore boundaries to the swash zone (e.g., Fiedler et al., 2019; Rutten et al., 2021). Obviously, non-negligible FIG energy contribution at the offshore boundaries would suggest possible underprediction of IG wave impacts based on the presently used forecast systems. Nearshore observations collected along open coasts (i.e., coastlines surrounding open oceans) provide indication for this possible underprediction by showing that the relative FIG energy contribution (at a water depth of O(10 m)) can be significant even under high swell energy conditions (Okihiro et al., 1992; Elgar et al., 1992; Herbers et al., 1995b). However, the relative energy contribution of the shoreward propagating FIG waves is largely unknown.

Analyses of FIG energy levels nearshore usually distinguish between energy of locally generated FIG (FIG_L) waves and energy due to remotely generated FIG (FIG_R) waves. The former represents IG energy radiation from nearby coasts, which may propagate shoreward if it is reflectively trapped (refer to recent review by Bertin et al., 2018), while the origin of the latter is principally unknown and is mostly explained based on radiation from remote shorelines (e.g., Webb et al., 1991; Rawat et al., 2014; Crawford et al., 2015; Neale et al., 2015; Tonegawa et al., 2018), although other possible generation mechanisms were proposed as well (e.g., Vrećica et al., 2019). Along open coasts, nearshore FIG energy is usually dominated by reflectively trapped energy (e.g., Smit et al., 2018), while FIG_R energy is typically negligible (e.g., Herbers et al., 1995b), after being diffused (due to, e.g., directional dispersion and refractive scattering in the presence of small-scale medium inhomogeneity) over transoceanic distances (i.e., distances of O(10 000 km)). However, beaches surrounding regional seas (for example, the North Sea, the Mediterranean Sea, the Gulf of Mexico) may be exposed to completely different IG conditions, since for such seas FIG_R waves travel much shorter distances (i.e., distances of O(100–1000 km)), and therefore, subject to much less energy density attenuation.

The importance of FIG_R waves in regional seas was recently demonstrated by Reniers et al. (2021), showing relatively high values of FIG wave heights in the middle of the North Sea under storm conditions. In order to explain these observations, Rijnsdorp et al. (2021) extended the SWAN model (Booij et al., 1999) with a parametrized source function proposed by Ardhuin et al. (2014) that describes short wave-driven FIG energy radiation along coastlines. Building on the agreement achieved between model and measured results, Rijnsdorp et al. (2021) used the SWAN model to investigate the importance of shoreward propagating FIG_R waves along the coastlines surrounding the North Sea. The model suggested that the relative energy levels of shoreward propagating FIG_R waves can demonstrate significant values depending on the storm and the examined nearshore location. As an example, storms blowing towards Denmark may result in incoming FIG wave heights near the Dutch coasts which are largely determined by IG waves radiated from the Danish coasts (see Fig. 5 by Rijnsdorp et al. (2021)).

Motivated by the results of Reniers et al. (2021) and Rijnsdorp et al. (2021), this study aims to further explore the potential importance of shoreward propagating FIG along the coasts of regional seas. To this end, the present study generalizes the predictive capabilities of FIG using SWAN and extends model verification for the North Sea. The new model developments and the extended model verification are made possible due to new data sets measured during the storm seasons of 2022 and 2023/24 at several offshore and nearshore locations over the southern North Sea. Compared to the measured data sets that formed the basis of the studies by Reniers et al. (2021) and Rijnsdorp et al. (2021), the present data sets have no upper limit on the IG frequency range (which was 0.01 Hz and has so far limited IG wave observations) and consist of a larger number of measurement points spread over a larger area over the southern North Sea (over water depths ranging from about 30 m to about 10 m). Such data availability allows generalizing and improving model calibration for the North Sea and the optimization and verification of its predictive capabilities for the full IG frequency range and over offshore and nearshore locations. Finally, in order to allow offshore as well as nearshore predictions with suitable spatial resolution, FIG wave modelling using SWAN is also extended to unstructured grids.

The new unstructured SWAN model for FIG waves over the North Sea is detailed in Section 2, whereas the new measurements are presented in Section 3. Based on the measured data, the model is optimized and verified in Section 4. Ultimately, the importance of FIG versus BIG energy nearshore is examined using the model and the available measurements in Section 5. Discussion and concluding remarks are outlined in Sections 6 and 7.

2. SWAN modelling of FIG waves over the North Sea

The SWAN model for FIG waves describes the evolution of IG energy in time and space due to refraction over varying bathymetry and dissipation through bottom friction. Using spherical coordinates, the model is mathematically defined through the following expression:

$$\frac{\partial E}{\partial t}+\frac{\partial c_\lambda E}{\partial \lambda}+\cos^{-1}\varphi\frac{\partial c_\varphi \cos\varphi E}{\partial \varphi}+\frac{\partial c_\sigma E}{\partial \sigma}+\frac{\partial \tilde{c}_\theta E}{\partial \theta}=-\chi\frac{\sigma^2}{g^2\sinh^2 kh}E \quad (1)$$

where $E(\sigma,\theta;\lambda,\varphi,t)$ is the space and time dependent spectral energy density, t represents time and c_λ, c_φ, c_σ and $\tilde{c}_\theta$ are the energy flux velocities through the longitude, latitude, frequency and direction spaces, respectively. Note that the expressions for the different flux velocities can be found in SWAN Team (2024). Additionally, the right-hand-side of (1) presents the expression for bottom friction, implemented here based on the formulation proposed by Hasselmann et al. (1973) for which the bottom friction coefficient, χ, is a constant. Finally, the bottom friction formulation also depends on the gravitational acceleration, g, the spectral wavenumber magnitude, k, and the water depth, h.

FIG energy is radiated into the model along source lines which are implemented parallel to the coastlines of the considered domain. The radiated energy arises because of two different sources. The first is the reflection of existing FIG waves which propagate towards the shore, while the second refers to the radiation of forced IG waves which are generated through nonlinear interactions and breaking of shoaling sea-swell waves. In order to model the first FIG source, SWAN defines a reflection parameter, R, which represents the ratio of outgoing and incoming FIG energy using values ranging from 0 to 1. The second source of energy is modelled in SWAN through the parameterization proposed by Ardhuin et al. (2014) that relates between the shoaling sea-swell waves and the reflected FIG waves as follows

$$E^0_{IG}=1.2\alpha^2\frac{kg^2}{c_g\sigma}\left(\frac{1}{4}H_{ss}T^2_{m-1,0}\right)^2\times F\times D \quad (2)$$

where $E^0_{IG}(\sigma,\theta)$ represents the seaward radiated FIG energy along the source lines, c_g is the group velocity, H_{ss} stands for the sea-swell significant wave height, $T_{m-1,0}$ represents the sea-swell mean wave period and α is a calibration parameter. Note that the present formulation uses $T_{m-1,0}$ instead of the originally proposed $T_{m-2,0}$ due to the unavailability of the latter within publicly accessible data of sea-swell waves, such as provided by Copernicus Marine Environment Monitoring Service (CMEMS). These two different characteristic periods are defined as $T_{m-1,0}=m_{-1}/m_0$ and $T_{m-2,0}=\sqrt{m_{-2}/m_0}$, where

$$m_n=\int_{f_{ss,min}}^{f_{ss,max}} f^n E_{ss}(f)\,df \quad (3)$$

and $[f_{ss,min}, f_{ss,max}]$ define the frequency range of the sea-swell energy spectrum E_{ss}. Finally, F represents the radiated frequency distribution and D stands for the radiated directional distribution.

The distribution functions F and D were proposed by Ardhuin et al. (2014) to follow specific universal forms. Here, the SWAN model is extended by generalizing these distribution functions. Over the frequency domain, the functional structure of F is preserved, but the fixed constants included in its definition are allowed to be tuned based on, e.g., field observations. Over the directional domain, the omnidirectional radiation proposed by Ardhuin et al. (2014) is generalized to allow for a preferable direction due to specular reflection. These functions are mathematically defined as

$$F = \frac{\left(\min(1, c_1/f)\right)^{c_2}}{\Delta_f}, \tag{4}$$

and

$$D = \begin{cases} \dfrac{\cos^m(\theta - \theta_{IG})}{\Delta_\theta}, & |\theta - \theta_{IG}| \le 90\,\text{deg} \\ 0, & |\theta - \theta_{IG}| > 90\,\text{deg} \end{cases} \tag{5}$$

The frequency distribution, F, is calibrated using the positive defined parameters c_1 and c_2. The calibration parameter for the directional distribution, D, is the positive defined power of the cosine, m, which controls the distribution width around θ_{IG}. The latter defines the expected FIG peak direction. This direction is evaluated based on the incident peak direction of the sea-swell waves under the assumption that the corresponding forced IG waves share the same directional peak and are specularly reflected from the coastline (see Herbers et al., 1995b,a; Reniers et al., 2010; Zhang, 2022; Nose et al., 2024). The value $m = 0$ (without the conditions on $|\theta - \theta_{IG}|$) descends the new definition of D back to the original omnidirectional definition of Ardhuin et al. (2014). Finally, Δ_f and Δ_θ ensure that both distributions integrate to 1.

In summary, the introduction above provides a general overview for the modelling of FIG waves using SWAN. In order to use SWAN over a specific domain, one would require to define specific source lines. These are considered next for the North Sea domain.

2.1. Definition of source lines for the North Sea

The source lines defined here for the North Sea (implemented over water depths of O(10 m)) are described in the right panel of Fig. 1. Each source line is assumed to be subjected to a different empirical relations between incoming sea-swell waves and outgoing FIG waves, as determined by α (see (2)). This source line division is considered since α is expected to strongly depend on the coastline characteristics. Specifically, two coastal characteristics are taken here into account for the classification between different source lines. These are the cross-shore slope and the bed material (see motivation for this choice by Herbers et al., 1995b; Van Dongeren et al., 2007). The distinction between milder and steeper cross-shore slopes are indicated by the right panel of Fig. 1 (based on global cross-shore slope data provided by Athanasiou et al., 2019). Yellow dots indicate coasts with milder slopes compared to coasts marked with black dots, showing that the source line of Belgium, the Netherlands and Germany characterize relatively milder average slope, while the source lines of north UK and Norway characterize relatively steeper average slope. Additionally, the bottom bed material contributed to the definition of the division shown for the source lines along the UK coasts. This division is based on the detailed description of the UK coastal bed material as presented by Fig. 1.2 in May and Hansom (2003). Thus, for example, the shorelines of northern UK and Shetland Islands, which are characterized by rocky coasts are distinguished from the shorelines of southern UK, which are characterized by sandy beaches. To conclude, these considerations led to the definition of the six source lines illustrated in Fig. 1 (refer to Section 2 of the Supplementary document for the specification of the source lines coordinates).

2.2. Unstructured SWAN modelling of FIG waves

Fig. 1 also describes a relatively coarse example of the depth-dependent unstructured grid type implemented for the FIG wave computation with SWAN. Generally speaking, the unstructured approach introduces some advantages over the nested approach, especially when considering problems involving wave evolution from offshore to nearshore locations. Specifically, unstructured grids provide flexibility to refine nearshore model resolution and to properly represent complex coastlines while maintaining cost-effective offshore coarse resolution in a single computational grid. By itself, such a possibility reduces modelling complexity compared to the nested approach. Moreover, the unstructured approach also avoids potential errors that could be caused by the nesting process and the introduction of internal boundaries and allows a built-in smooth exchange of information between coarser and finer computational regions.

The unstructured grid implemented here is generated using the recently developed MATLAB-based mesh generation code called OceanMesh2D (Roberts et al., 2019). Besides refinement nearshore, OceanMesh2D also allows grid refinement according to bathymetry levels, so that finer resolution is applied over shallower areas in the North Sea (see, e.g., the finer grid resolution over the Doggersbank in the left panel of Fig. 1). This is implemented by specifying the number of elements N per semi-diurnal tidal wavelength λ_{M2} as

$$\Delta x = \frac{T_{M2}\sqrt{gh}}{N} \tag{6}$$

where the dependence of λ_{M2} on depth is explicitly expressed by the numerator on the right-hand-side of (6) using the shallow water dispersion relation, and T_{M2} is the semi-diurnal tidal wave period (equal to about 12.42 h). Here, N is taken to be $N = 250$ which results in a grid resolution of about 5 km over 80 m depth in the northern parts of the North Sea and grid resolutions of about 1.75–3 km over 10–30 m depths in the southern parts of the North Sea. Additionally, for deeper depths, the maximum resolution is limited to 10 km. Nearshore, it is restricted to 0.5 km. Finally, note that the model is configured here with a directional resolution of 5° and 37 logarithmically spaced discrete frequencies ranging from 0.0025 Hz to 0.075 Hz.

2.3. Nearshore parameters of sea-swell waves

Lastly, it is also necessary to specify the sea-swell wave parameters in order to allow energy generation of FIG along the source lines surrounding the North Sea, as dictated by (2). To this end, publicly accessible wave data were downloaded from a CMEMS product called the Atlantic-European North West Shelf-Wave Physics Reanalysis. This product provides hindcast of wave parameters for waves with periods of 3–30 s. The model underlying this product is WAVEWATCH III (WW3) (Tolman et al., 2009), computed with spatial resolution of about 1.5 km and temporal resolution of 3 h, and with atmospheric forcing provided by the ECMWF ERA5 reanalysis data. For the purposes of the present study, the spatio-temporal accuracy of the sea-swell wave data is particularly important nearshore, as it affects the accuracy of FIG wave generation along the source lines, and therefore, the prediction capabilities of FIG waves. The nearshore accuracy of the presently used CMEMS product, which hereafter will be referred as WW3, is examined in the Supplementary document. This examination and the verification of the newly developed unstructured SWAN model to predict FIG waves in the North Sea are based on a new collection of wave observations which are described in detail in the next section.

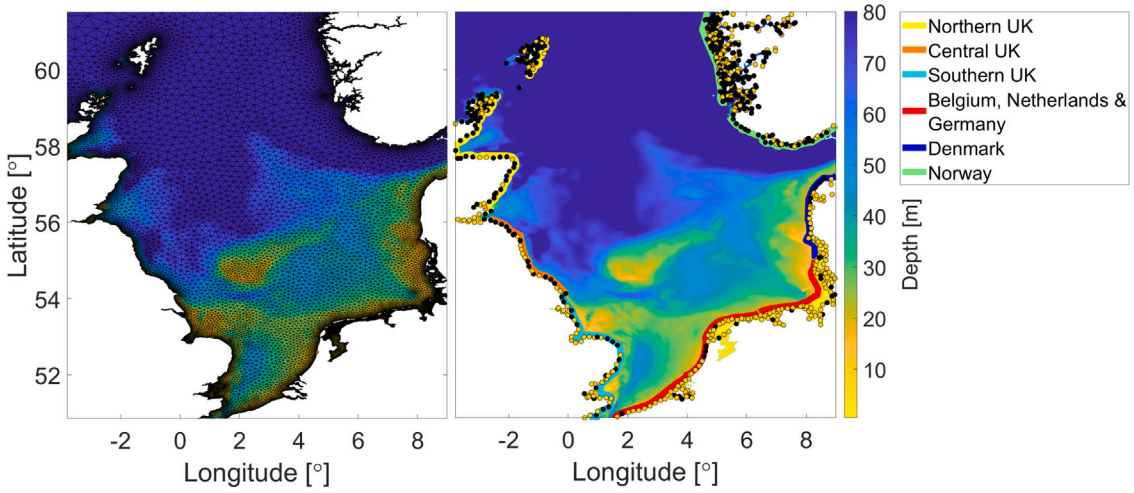

Fig. 1. The definition of the source lines (right panel) and a relatively coarse example of the depth-dependent unstructured grid (left panel) used for the SWAN modelling of FIG waves over the North Sea. The black and yellow dots shown in the right panel define coasts with a cross-shore slope steeper and milder than 1/120, respectively.

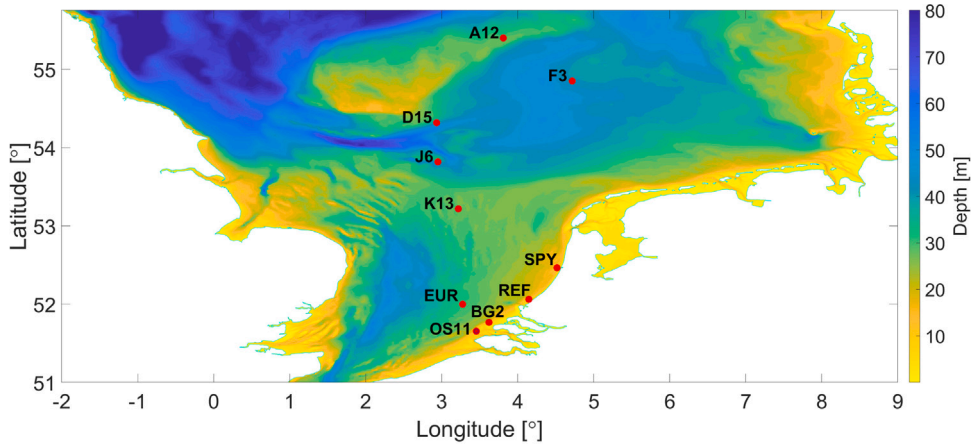

Fig. 2. Measurement stations (indicated by the red dots) over the southern North Sea.

Table 1
Specifications of the measurement stations. The observations were collected between January and April 2022 ("SP22") and between October 2023 and February 2024 ("SP23/24"). Data availability per station is indicated in the last column. Additionally, the available information of radar heights ([m] above MSL) are included in parentheses in the "Instrument" column.

Name	Lat [°]	Long [°]	Depth [m] (MSL)	Instrument (Radar height [m])	Sampling frequency [Hz]	Availability
OS11	51.643	3.480	10.0	Radar	2.56	SP22 & SP23/24
BG2	51.767	3.622	10.6	Step gauge	2.56	SP22 & SP23/24
EUR	51.998	3.275	32.3	Radar (14.0)	2.56	SP23/24
REF	52.061	4.146	13.3	Pressure gauge	4	SP22
SPY	52.464	4.517	18.3	Radar (12.1)	2.56	SP22 & SP23/24
K13	53.217	3.219	29.0	Radar (24.2)	2.56	SP22 & SP23/24
J6	53.817	2.950	42.1	Radar (29.1)	2.56	SP23/24
D15	54.317	2.933	42.1	Radar (17.8)	2.56	SP23/24
F3	54.850	4.717	42.9	Radar	2.56	SP23/24
A12	55.399	3.810	30.3	Radar (26.3)	2.56	SP22

3. Wave observations in the southern North Sea

The present study presents recent field observations of waves over the southern North Sea at the locations shown in Fig. 2. The observations were collected using different instruments and during different time periods. A summary of the specifications for each measurement point is detailed in Table 1.

The measuring instruments used to collect the observations discussed here are platform-mounted radars looking downward from about 10–30 m above MSL, a step gauge which is a pole with a number of equidistant electrodes that is fixed to the sea bed, and a pressure gauge near the bed. These instruments provide discrete time series of the surface elevation, and therefore, allow to reconstruct one-dimensional frequency dependent energy spectra and the corresponding wave parameters such as H_{m0} and $T_{m-1,0}$.

The observations considered here are divided into two storm periods, the period between January and April 2022 (denoted hereafter as "SP22") and the period between October 2023 and February 2024

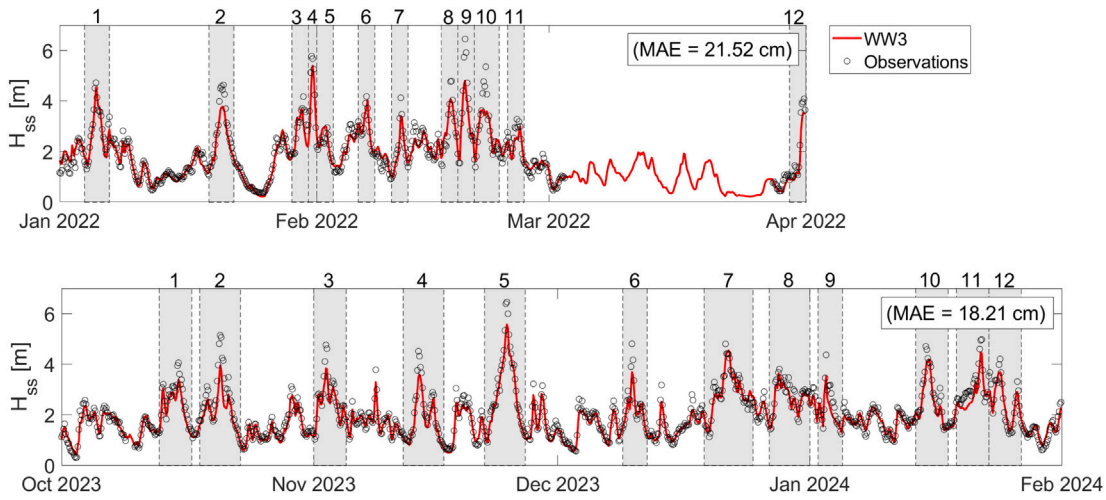

Fig. 3. Observed (circles) and WW3 predicted (solid red line) H_{ss} at the measurement station K13 during SP22 (upper panel) and SP23/24 (lower panel). The gray bands define the periods of the storms considered in this study. The names of the storms are listed in Table 2 and are indicated here by the corresponding storm numbers appearing at the top of the gray bands. Also included is the mean absolute error (MAE) of the WW3 prediction with respect to the observations (see the MAE values in parentheses at the upper right corners of the two panels).

Table 2
Names of storms during SP22 (left) and SP23/24 (right). In conjunction with Fig. 3, the numbers attached to the names indicate when the storms occurred. Additionally, the ERA5 maximum hourly sustained wind speed during the storm peak is given under the "Wind speed" column. Finally, a general overview of the ERA5 wind directions during the storm peak is provided in terms of the most impacted coastlines under the "Impacted coasts" column, where the notation "-" indicates counterclockwise inclusion (e.g., BE-NOR refers to all coastlines from Belgium to Norway in counterclockwise order around the North Sea).

SP22				SP23/24			
No.	Name	Wind speed [km/h]	Impacted coasts	No.	Name	Wind speed [km/h]	Impacted coasts
1	Jan 5	69	BE-DK	1	Oct 15	69	GER-NOR
2	Jan 20	71	GER-NOR	2	Babet	89	UK
3	Corrie (a)	87	GER-NOR	3	Ciarán	67	NOR
4	Corrie (b)	80	BE-NL	4	Debi	67	NL-GER
5	Corrie (c)	68	GER-NOR	5	Nov 24	71	BE-NOR
6	Feb 7	69	BE-NOR	6	Elin	64	NL, UK
7	Feb 11	66	NL-NOR	7	Pia	83	NL-NOR
8	Dudley	78	NL-DK	8	Gerrit	80	DK, UK
9	Eunice	79	BE-DK	9	Henk	83	NL-GER, UK
10	Franklin	65	BE-DK	10	Irene	65	UK-NOR
11	Feb 25	68	GER-DK	11	Isha	76	GER-NOR
12	Mar 31	45	UK-NL	12	Jocelyn	69	NL-NOR

(denoted hereafter as "SP23/24"). As detailed in Table 1, only a few stations collected wave measurements during both of these storm periods. In total, 6 stations collected wave measurements during SP22 (i.e., "OS11", "BG2", "REF", "SPY", "K13" and "A12") and 8 stations collected wave measurements during SP23/24 (i.e., "OS11", "BG2", "EUR", "SPY, "K13", "J6, "D15", and "F3").

Based on the raw data produced by the different stations (given as time series sampled according to the frequencies listed in Table 1), three-hourly time series are generated. At each time step, a conventional spectral and bispectral analysis is performed (see details by Herbers et al., 1994, and refer to a brief summary in the Supplementary document) using semi-overlapping blocks of 10 min to evaluate sea-swell and IG wave parameters and to separate BIG from FIG energy contributions. The bulk results are classified into sea-swell waves with periods of 3–30 s and infragravity waves with periods of 30–200 s.

Fig. 3 shows the results of the sea-swell significant wave height at station K13 (a station located in the central North Sea, as described by Fig. 2). On top of these results are gray bands representing the various storms that occurred during SP22 and SP23/24. The numbers at the top of the bands correspond to the storm names listed in Table 2. The storms considered include both officially named storms (given by the meteorological institutes Met Office, Met Éireann, and the Royal Netherlands Meteorological Institute) and unnamed storms (which are labelled according to their peak date, e.g., storm Jan 5). These storms were selected based on their associated significant wave heights (reaching close to or exceeding 4 m at K13, as shown in Fig. 3) and sustained wind speeds (reaching close to or exceeding 65 km/h, according to Table 2, with the exception of storm Mar 31). In addition, the duration of each storm (shown by the gray bands in Fig. 3) was determined using ERA5 hourly wind velocity time series (Hersbach et al., 2023). These time series clearly illustrate the intensification and weakening of wind speeds over the North Sea basin, allowing the storm periods to be readily identified. Finally, Fig. 3 also compares between observed and modelled sea-swell wave heights. The close match shown between the WW3 prediction and the observations is also verified by the mean absolute error (included in the upper right corner of each panel in Fig. 3), defined as

$$\mathrm{MAE} = \left\langle \left| H_{ss}^{obs} - H_{ss}^{m} \right| \right\rangle \tag{7}$$

where $\langle \ldots \rangle$ indicates time averaging, and the superscripts obs and m indicate observed and modelled values, respectively.

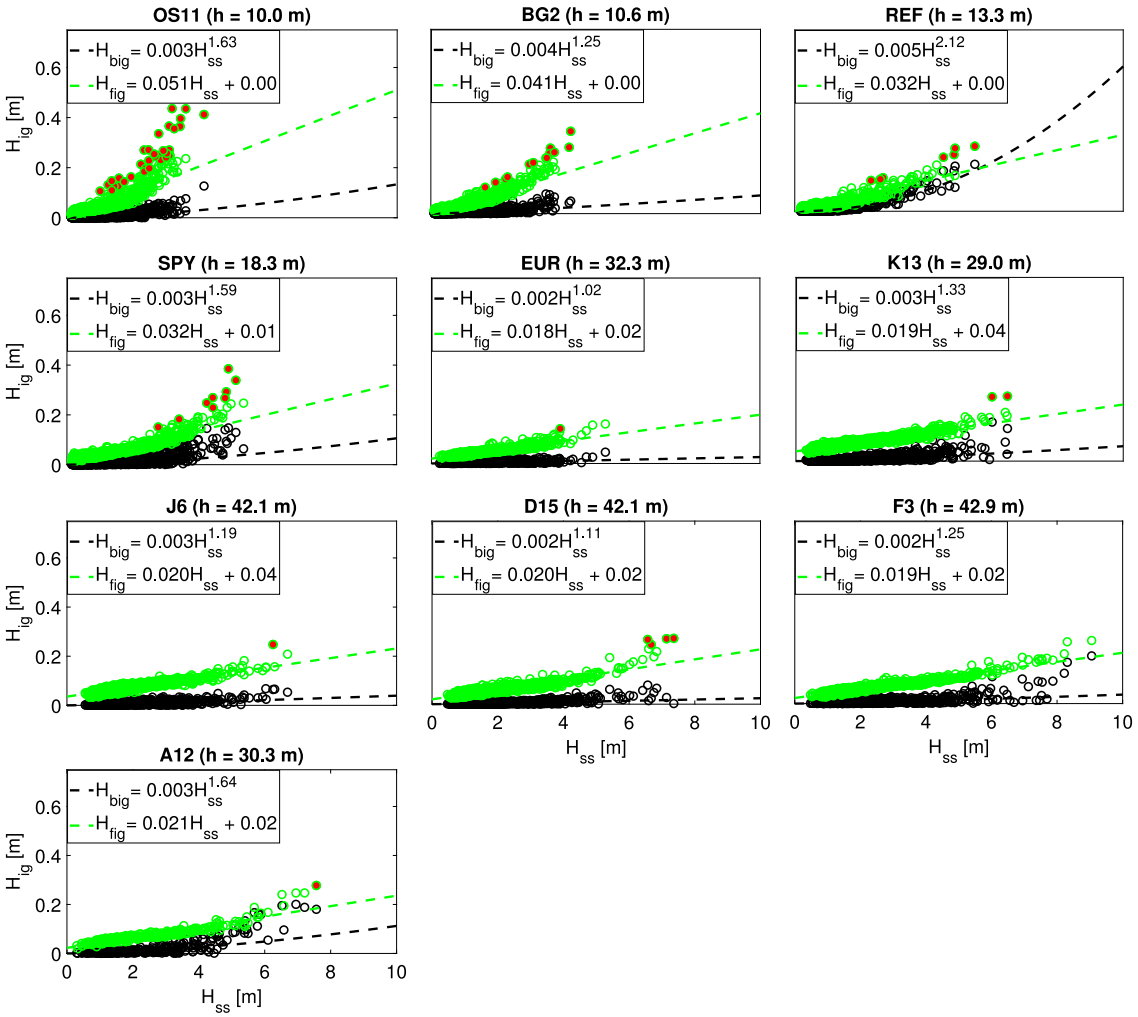

Fig. 4. H_{ig} observations as a function of H_{ss} during SP22 and SP23/24. Green circles denote H_{fig} observations and black circles are the observations of H_{big}. The dashed lines are fitting curves whose expressions are given at the upper part of each panel. The red fill of some of the green circles indicates H_{fig} observations which are higher than 0.1 m and 1.5 times higher than the expected fit. For convenience, the water depths, h, of the different stations are included in parentheses.

3.1. BIG and FIG wave observations over the southern North Sea

Besides the sea-swell components, the measurements at the different stations considered here also allow to extract the IG signals and to distinguish between the BIG components which are nonlinearly coupled to the sea-swell waves and the FIG components which are freely propagating in space. Fig. 4 summarizes the observations of H_{ig} as a function of H_{ss} for each of the stations. During storm conditions, H_{ss} is observed to approach almost 10 m height offshore (as demonstrated by station F3), whereas nearshore, the highest sea-swell waves reach values between 4 m (see, e.g., H_{ss} values of OS11) and 6 m (as seen, e.g., by station REF). In contrast to the sea-swell heights, the IG heights become higher nearshore compared to offshore and can reach almost 0.5 m height (as demonstrated by H_{fig} at OS11).

Fig. 4 also presents the functional relations of H_{fig} and H_{big} with H_{ss}, using fitting curves with predetermined functional structures. Herbers et al. (1995b) showed that for open coasts (i.e., coastlines surrounding open oceans) these relations obey to the following expressions:

$$H_{big} \propto H_{ss}^2 \tag{8}$$

$$H_{fig} \propto H_{ss} \tag{9}$$

Accordingly, the structures of the fitting curves are chosen to follow the expressions pH_{ss}^q and $aH_{ss} + b$, to represent the values of H_{big} and H_{fig} respectively, with the aim of examining the validity of the findings by Herbers et al. (1995b) to offshore and nearshore conditions in the North Sea. The fitting curves obtained for each of the stations are summarized by the panels of Fig. 4. It is observed that q tends to the expected value of 2 only for some of the stations while for most of the stations the values of q are quite low (see, e.g., the fits of EUR, J6 and D15). The reasons for these observations can be physically related (e.g., due to time dependent frequency or directional spreading of the sea-swell waves which may lead to significant scatter in the relation between H_{big} and H_{ss}) or related to the measurement accuracy of IG waves (the measurement accuracy of low-frequency heights using radars may be exposed to deviations as demonstrated by Ewans et al., 2014; Jangir et al., 2022). Low q values are also obtained for the step gauge station BG2, while the results of the pressure gauge at station REF are consistently follow the excepted theoretical value of $q = 2$.

Inaccuracy of IG measurements may also be the cause of non-zero b value of the H_{fig} fit. This b value essentially represents the value of H_{fig} for $H_{ss} = 0$. Non-zero b values appear for radar stations and are particularly high for offshore stations, while for nearshore stations b tends to zero. A plausible explanation for the divergence of b from zero for offshore radar stations is the dependency of the radar performance on its height above the mean sea level (and its associated footprint as explained by Jangir et al., 2022), where this height is usually greater for offshore versus nearshore stations (see also the available radar heights in Table 1). Indeed, a weak support for this explanation is observed by

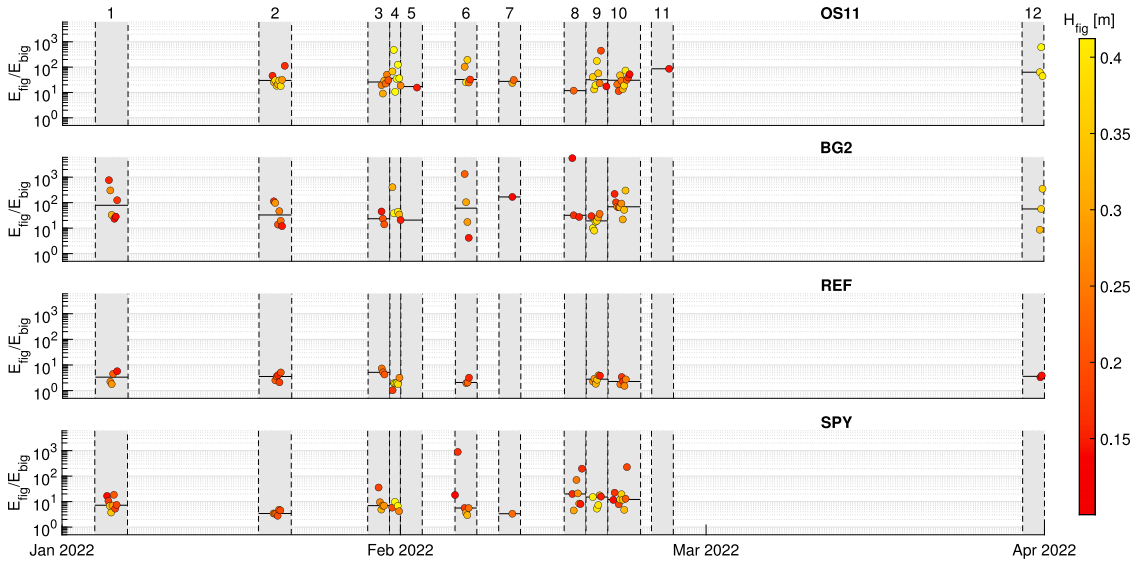

Fig. 5. Energy ratios of FIG and BIG waves (circles) at nearshore stations and under storm conditions (conditions for which $H_{fig} > 0.1$ m) during SP22. The medians of the energy ratios during the different storms (the numbers on top of the upper panel indicate the storm names according to Table 2) are plotted by the short horizontal black lines. The face colour of the circles indicates the value of H_{fig} according to the colour bar on the right side of the panels.

examining the different b values in conjunction with the available radar heights (where the rather high positioned radar at A12 can be seen as an outlier). Additionally, it seems that b may subject to different values for nearby stations with similar depth conditions (see the b values of stations J6 and D15). This observation suggests that b may be affected by a local factor, and thus, supports the possibility of measurement error.

The results presented by Fig. 4 also allow to qualitatively compare between the heights of the FIG and the BIG components. Generally speaking, the results suggest that the FIG energy is more significant than the BIG energy over both offshore and nearshore regions and for most of the sea-swell wave conditions. However, for some of the locations and for high H_{ss} values, H_{fig} and H_{big} tend to become comparable (see, e.g., the results of stations REF, SPY, F3 and A12). This tendency is consistent with the observations of Herbers et al. (1995b) for open coasts. Yet, the present results also reveal scenarios with high H_{ss} values for which the FIG wave heights are significantly higher than those of the BIG waves. Some of these scenarios seem to coincide with the H_{fig} observations which are indicated by the red fill, namely with cases for which H_{fig} is 1.5 times higher than the expected fit (see the red fill of some of the green circles in Fig. 4). Finally, it is noted that these scenarios are mostly observed at nearshore stations (see, e.g., the highest H_{fig} results of OS11).

One of the explanations for the H_{fig} deviations from the expected fit at nearshore locations and for high H_{ss} is the dependency of the shoreline reflected FIG energy on the mean sea-swell wave period as observed by Ardhuin et al. (2014) who suggested to improve the linear fit (i.e., aH_{ss}) with $aH_{ss}T^2_{m-2,0}$. Indeed, the latter was recently observed by Oh et al. (2023) to correlate better with high H_{fig} values nearshore compared to the correlation achieved with the former. Additional explanation for the higher than expected H_{fig} nearshore could be the release of BIG waves due to sea-swell wave breaking or due to rapid bathymetry changes. This effect is particularly expected for high H_{ss} values and over nearshore regions characterized by significant bathymetry changes (as demonstrated by the bathymetric structure in front of stations OS11 and BG2). Among the other possible explanations for high H_{fig} values nearshore which deviate significantly from the linear fit, and at the same time show values that are much more significant than the corresponding H_{big} values, is the contributions of FIG_R waves that are uncorrelated to H_{ss}. In contrast to open coasts for which energy due to FIG_R waves is diffused over transoceanic distances, over regional seas like the North Sea, FIG_R waves travel distances that may be one or two orders of magnitude shorter, and thus, their nearshore energy can potentially be much more significant. In order to explore more indications that can support this hypothesis, the following subsection examines in further detail the relative importance of FIG waves nearshore and under storm conditions.

3.2. The relative importance of nearshore FIG waves under storm conditions

The importance of FIG waves nearshore is examined here based on the energy ratio of FIG and BIG waves at stations OS11, BG2, REF and SPY as a function of time. The present examination focuses on storm conditions which satisfy $H_{fig} > 0.1$ m. Figs. 5 and 6 show that the nearshore medians of the energy ratios are always higher than one under storm conditions, and for some of the stations and storms can even reach higher values than a hundred (see, e.g., the results of OS11 and BG2).

Based on observations at open coasts (e.g., Elgar et al., 1992; Herbers et al., 1994, 1995b), it is expected that the energy ratio will be lower for higher H_{ss}, and thus, higher H_{fig} (recall (8) and (9)). This inverse relation indeed appears by comparing between the energy ratios and H_{fig} in Figs. 5 and 6 for stations REF and SPY. On the other hand, the existence of this relation does not hold for stations OS11 and BG2 (see for example the relatively high energy ratio obtained for Corrie (b) (storm number 4 of SP22), which resulted in the highest H_{ss} during SP22). Additionally, observations at open coasts also suggest that under storm conditions and for relatively shallow waters, the energy ratios are expected to be close to 1 or may even be smaller (e.g., Elgar et al., 1992; Herbers et al., 1994, 1995b), or alternatively, that under such conditions, the relative contribution of E_{big} becomes significant. However, the present nearshore observations at the North Sea demonstrate higher energy ratios than the expected outcomes from open coasts. Specifically, stations OS11 and BG2, which demonstrate energy ratios that are order of magnitude higher than those of stations REF and SPY, suggest that the E_{big} under storm conditions remains insignificant compared to E_{fig}.

Additional information that can help explain the high energy ratios observed nearshore in the North Sea under storm conditions is extracted from the spatial distribution of the horizontal wind field (i.e., $\boldsymbol{U_{10}}$) at the storm peaks. Six such examples are shown in Fig. 7. In general, North Sea storms are associated with northwesterly winds

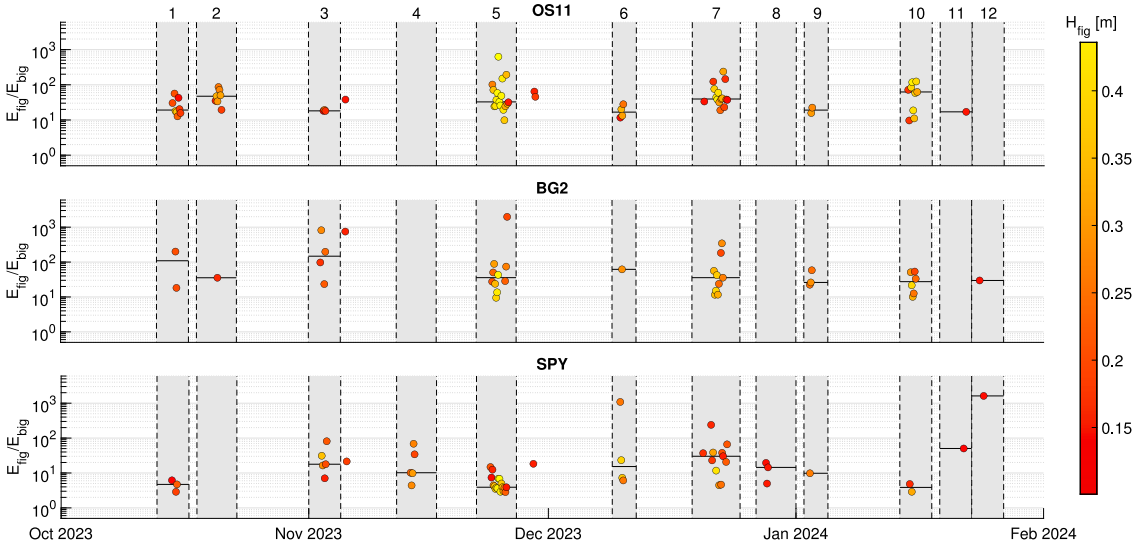

Fig. 6. Energy ratios of FIG and BIG waves during SP23/24 (see the caption of Fig. 5 for detailed specification).

(as also suggested by the impacted coasts in Table 2), and therefore, significant FIG energy is expected to radiate seaward from the coasts of DK and GER (as also observed by Rijnsdorp et al., 2021). An exceptional wind direction observed during Corrie (b) (storm number 4 of SP22), which blew directly towards the nearshore stations REF and SPY, leading to the highest FIG wave response measured during SP22. In contrast, during Corrie (a) (storm number 3 of SP22), higher wind speeds were observed (see also wind speeds in Table 2) but these were directed towards DK, leading to lower H_{fig} response and generally higher energy ratios (compare, e.g., the energy ratios of REF during Corrie (a) and (b) in Fig. 5). Besides the possible low relative contribution of E_{big}, the reason for the relatively high energy ratios during Corrie (a) could also be the relative energy contribution of FIG_R waves, which in this case is expected to arrive from the coasts of DK and GER. A stronger indication to the energy contribution of FIG_R waves is provided through the case of storm Babet (storm number 2 of SP23/24). This storm presents an unusual easterly wind, and thus, expected to be followed by seaward radiation of FIG waves along the UK coasts. During storm Babet, the wind speeds (as described by Fig. 7) and H_{ss} values (as observed in the Supplementary document by Fig. 2) at nearshore stations are relatively low. Accordingly, local responses of H_{fig} at these locations during storm Babet are expected to be relatively low as well. However, Fig. 6 shows rather significant H_{fig} values at station OS11. These values are also accompanied by very high energy ratios. Therefore, it is reasonable to assume that these results were obtained due to significant FIG energy contributions originating from the coasts of UK.

In summary, the FIG energy contribution is found to be significantly more dominant than the BIG energy contribution at nearshore stations and under storm conditions. Particularly high energy ratios were observed over the more sheltered (less exposed to strong wind velocities and the associated higher sea-swell waves) stations OS11 and BG2. These ratio values effectively suggest that the contributions of BIG waves at OS11 and BG2 are negligible under storm conditions. Additionally, it is also attempted here to extract indications which point towards the importance of the nearshore energy contribution due to FIG_R waves. However, these indications are rather weak and cannot be used to draw concrete conclusions. This statement emphasizes the limited capability of understanding the dynamics of FIG waves in the North Sea based on the observations presented here. Specifically, the observations do not allow gaining insights into the relative energy contribution of shoreward propagating FIG waves, nor into the importance of energy contribution due to FIG_R waves. Nevertheless, this information is essential because it may indicate the possibility of underestimation of the coastal impacts due to IG waves as obtained based on current engineering practice which neglects the FIG wave contribution.

In contrast to the observations, the unstructured SWAN model developed in Section 2 allows estimating the contribution of the shoreward propagating FIG waves and the importance of the FIG_R waves. To ensure reliable model assessments, the following section is devoted to optimize and verify model performance to predict FIG wave dynamics in the North Sea.

4. Model optimization and verification

4.1. Optimization

The model optimization aims to find the parameter values which optimize model performance with respect to the observations discussed in Section 3. These parameters include c_1, c_2 and m which determine the functional structure of the FIG energy distribution radiated along the model source lines (see (4) and (5)) and the alpha parameters α_{ukn}, α_{ukc}, α_{uks}, α_{bng}, α_{dk} and α_{nor} which determine the intensity of the FIG energy radiation along the Northern UK coast, the Central UK coast, the Southern UK coast, the coasts of Belgium, the Netherlands and Germany, the Denmark coast and the Norway coast, respectively (see also the right panel of Fig. 1). Additional parameters are χ and R which determine the significance of the bottom friction and the shoreline reflection.

4.1.1. The spectral distribution parameters of FIG waves

Since observations of the directional properties of FIG waves are not available along the different coasts of the North Sea, the value chosen for m is $m = 0$, which corresponds to the omnidirectional assumption. This choice is supported by the linear result which states that for alongshore uniform and mildly sloping beach, the directional distribution of (refractively trapped) seaward radiating FIG waves converges to a constant far enough from the shoreline and independent of the directional structure at the shoreline (see Herbers et al., 1995b). Yet, deviations from this omnidirectional assumption are anticipated (see, as an example, the observations by Herbers et al., 1995b, Fig. 6) due to the irregular lateral structure that characterizes various North Sea coasts and since the source lines are quite adjacent to most of the shorelines.

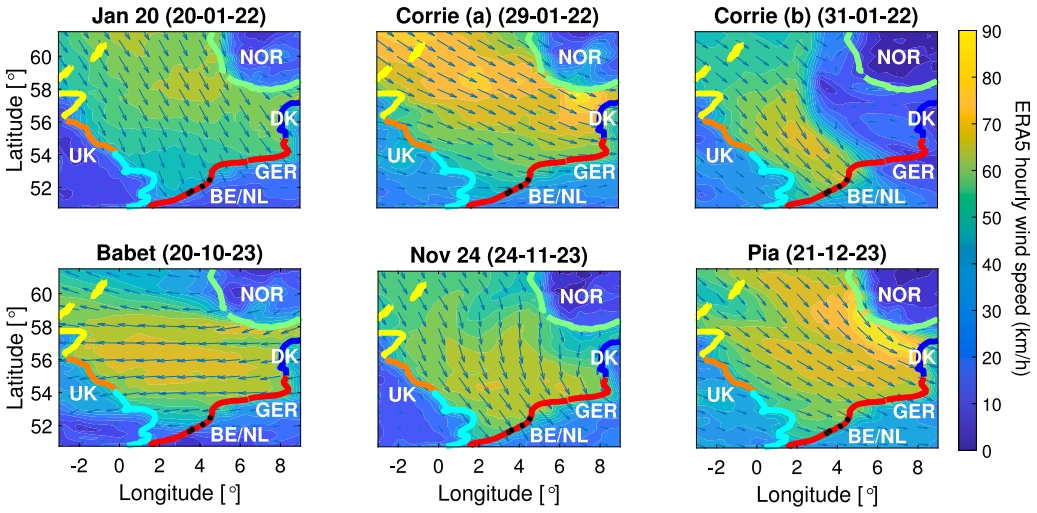

Fig. 7. Horizontal wind field (i.e., $\boldsymbol{U}_{10}$) at storm peaks over the North Sea as provided by ERA5 hourly wind velocities (Hersbach et al., 2023). The coasts surrounding the North Sea are illustrated by the coloured lines and the four black dots indicate the station locations, from left to right OS11, BG2, REF and SPY.

In contrast to the parameterization for the directional distribution, the parameterization for the frequency distribution benefits from limited data availability. Specifically, an averaged structure of nearshore IG frequency distribution can be extracted based on the observations of stations OS11, BG2, REF and SPY. Mathematically, this averaged structure is written as

$$F^{obs} = \frac{1}{\sum_j N_j} \sum_j \sum_{t \in \tau_j} \frac{E_{ig}^j(f,t)}{m_{0,ig}(t)} \tag{10}$$

where j indicates the nearshore station, τ_j is the set of times for which data are available at station j and N_j is the element number within set τ_j. Additionally, E_{ig}^j is the energy density of the IG range at location j and $m_{0,ig}$ is the zero-order moment of that energy density. Note that F^{obs} essentially characterizes the complete IG field including the bound and the free components. In addition, it does not distinguish between waves with different directions of propagation. Finally, F^{obs} characterizes the frequency distribution of IG waves near the Netherlands coasts only. Therefore, the use of F^{obs} as a reference to calibrate the frequency distribution imposed in the model effectively assumes that the BIG energy is generally negligible compared to the FIG energy, the frequency distribution of the seaward and shoreward propagating FIG waves has similar structure and that this structure approximately characterizes all the coasts surrounding the North Sea. Based on these assumptions (which receive merely a partial confirmation through the BIG and FIG wave observations presented in Section 3), the c_1 and c_2 values which provide the optimal fit between the F defined in (4) and F^{obs} are:

$$c_1 = 0.017 \text{ [Hz]} \tag{11}$$

$$c_2 = 0.3 \tag{12}$$

Especially notable is the difference between the value of c_2 that is found here and the values of 1 or 1.5 suggested by earlier studies (Godin et al., 2013; Ardhuin et al., 2014; Zheng et al., 2021). This difference indicates the spatial dependence of this parameter, which results from the different typical conditions at different locations across the globe.

4.1.2. FIG parameters for energy generation, reflection and dissipation

The FIG parameter values for energy generation (i.e., the alpha values), reflection (i.e., the value of R) and dissipation (i.e., the value of χ) are found as follows. As a first step, a calibration period is decided. This period is selected to be from 24 October to 27 November of 2023. The reasons behind this choice are the availability of observations at a relatively large number of stations (including offshore and nearshore stations) and because during this period there were several fairly strong storms (i.e., Ciarán, Debi and Nov 24) which were characterized by strong wind speeds along most of the North Sea coastlines (as described by the time series of the ERA5 hourly wind velocities). Thus, this period is expected to involve significant contributions of FIG energy due to most of the source lines. Secondly, based on observations of earlier studies (i.e., Rijnsdorp et al., 2021; Fa, 2021), a set of 12 pairs of χ, R values are defined. This set is obtained through the different choices out of the following ranges:

$$\chi \in [0.005, 0.01, 0.02] \tag{13}$$

$$R \in [0, 0.25, 0.5, 1] \tag{14}$$

In the third step, an optimization process is performed for each value pair of χ, R to find the alpha vector (i.e., $\boldsymbol{\alpha} = [\alpha_{ukn}, \alpha_{ukc}, \alpha_{uks}, \alpha_{bng}, \alpha_{dk}, \alpha_{nor}]$) that leads to the most favourable model results with respect to the observations. In order to obtain a solution which adequately describes offshore and nearshore FIG wave dynamics, the calibration of $\boldsymbol{\alpha}$ is based on two offshore and two nearshore stations. The selected stations are BG2, SPY, D15 and F3. Besides their locations, these stations were chosen since their measurements seem relatively reliable based on the assumption that the FIG fit parameter b should be rather small (see Fig. 4). Finally, the optimization process itself is explained by the following. From the set of time points that defines the calibration period, 16 time points are randomly chosen for each of the four selected stations. This results in a random set of 64 points, based on which, a gradient descent is performed to extract a realization of $\boldsymbol{\alpha}$ that minimizes the error produced by the model. The model error is defined as follows:

$$error = \sum_{t_i} |E_{fig}^{obs} - E_{fig}^{m}| \tag{15}$$

where

$$E_{fig}^{m} = \sum_n \alpha_n^2 E_{fig,n}^{m} \tag{16}$$

and $E_{fig,n}^{m}$ is the spatial energy distribution at time t_i due to $\alpha_n^2 = 1$, while setting the other alpha values to zero. Note that this expansion in terms of the different source line contributions is possible due to the linearity of (1) in $E(\sigma, \theta; \lambda, \varphi, t)$. Additionally, E_{fig}^{obs} is the observed energy distribution at time t_i. Ultimately, the average of different $\boldsymbol{\alpha}$ realizations is obtained by repeating this optimization method using different random sets of time points. A summary of the model performance for each pair of χ, R is detailed in the Supplementary document. Finally, $\boldsymbol{\alpha}$ is selected based on the results of $\chi = 0.02$ m^2 s^{-3} and $R = 0.25$. These $\boldsymbol{\alpha}$ values are presented in Table 3.

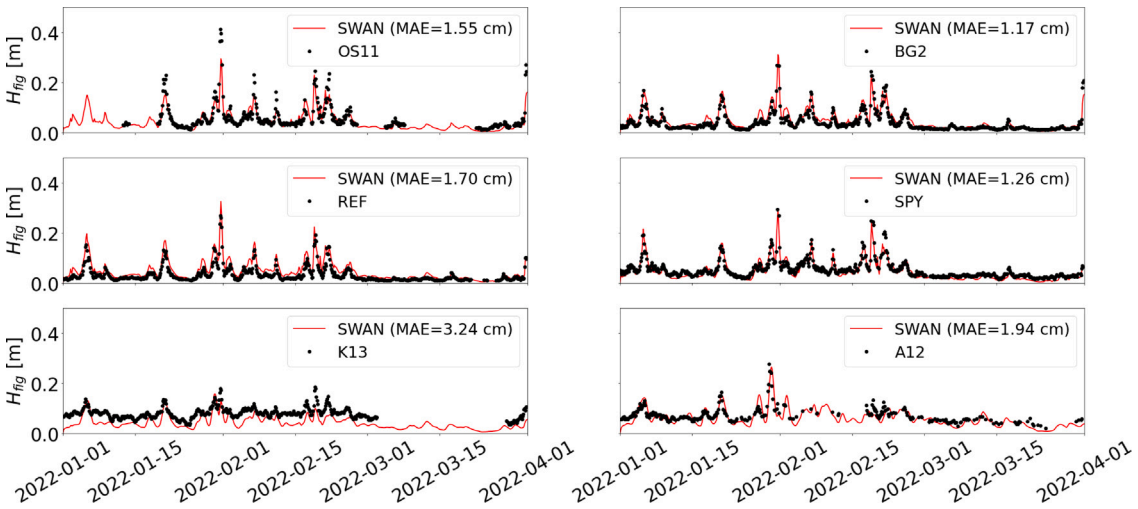

Fig. 8. Observed (black dots) and modelled (red line) H_{fig} during SP22. The mean absolute error (MAE) of the model with respect to the observations is provided in parentheses at the upper right corner of each panel.

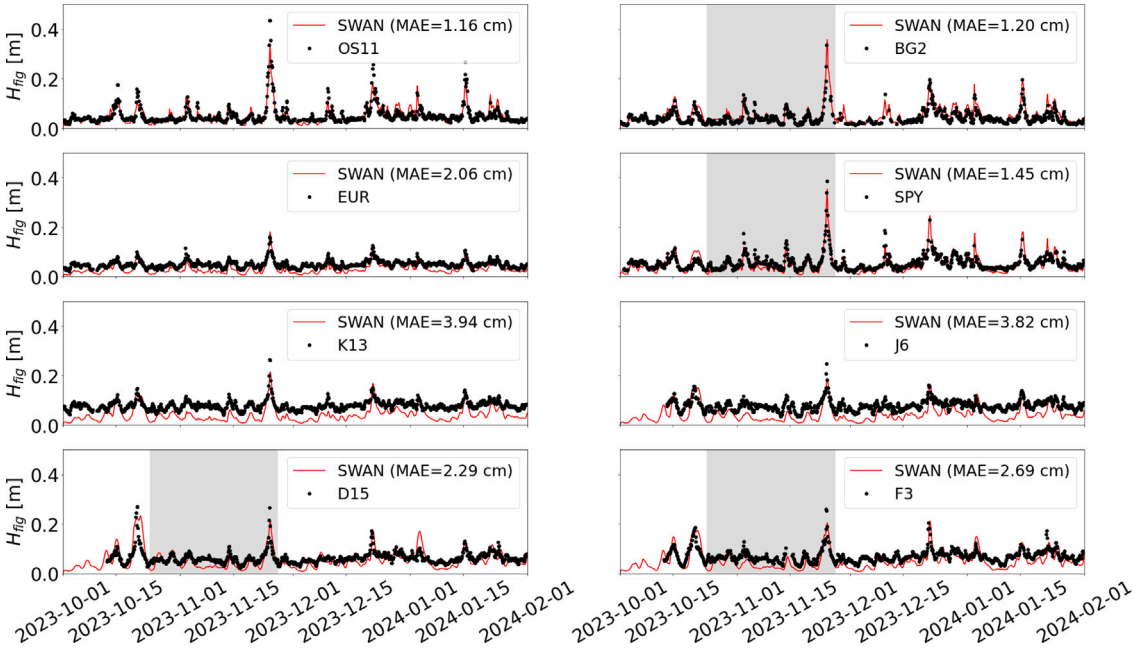

Fig. 9. Observed (black dots) and modelled (red line) H_{fig} during SP23/24. The mean absolute error (MAE) of the model with respect to the observations is provided in parentheses at the upper right corner of each panel. Additionally, the gray backgrounds indicate the observations used to optimize $\boldsymbol{\alpha}$.

4.2. Verification

The model verification is based on observations which were not used for the calibration of $\boldsymbol{\alpha}$. For convenience, the observations assigned to optimize $\boldsymbol{\alpha}$ are indicated using the gray backgrounds in Fig. 9. Therefore, the rest of the observations are used here for verification. The verification is presented by comparing the model predicted H_{fig} with the H_{fig} observed during SP22 (see Fig. 8) and during SP23/24 (see Fig. 9). Additionally, similar comparisons are considered for the characterized IG period and frequency distribution in the Supplementary document.

The comparisons in Figs. 8 and 9 show that the MAE of the model prediction (calculated according to (7)) ranges from about 1 cm to about 4 cm. Generally, the MAE of nearshore stations is typically low. Yet, a consistent model overprediction appears at station REF, which results in a relatively high MAE nearshore (see also model performance assessment in Appendix A). This high MAE value may be due to the fact that the calibration of $\boldsymbol{\alpha}$ relies on different instruments (i.e., radar and step gauge) than that of REF, which may systematically estimate higher IG estimates than the REF instrument (i.e., pressure gauge). Additionally, the model underpredicts the relatively high H_{fig} values at OS11. This underprediction may partly result from OS11 being modelled slightly seaward of its actual location. This adjustment was made because the source lines pass directly in front of (and seaward of) the OS11 station, thus OS11 is located outside the computational

Table 3
The $\boldsymbol{\alpha}$ values (with dimension s^{-1}) obtained for $\chi = 0.02$ $m^2 s^{-3}$ and $R = 0.25$.

α_{ukn}	α_{ukc}	α_{uks}	α_{bng}	α_{dk}	α_{nor}
27.88×10^{-4}	20.26×10^{-4}	14.10×10^{-4}	14.57×10^{-4}	18.36×10^{-4}	20.75×10^{-4}

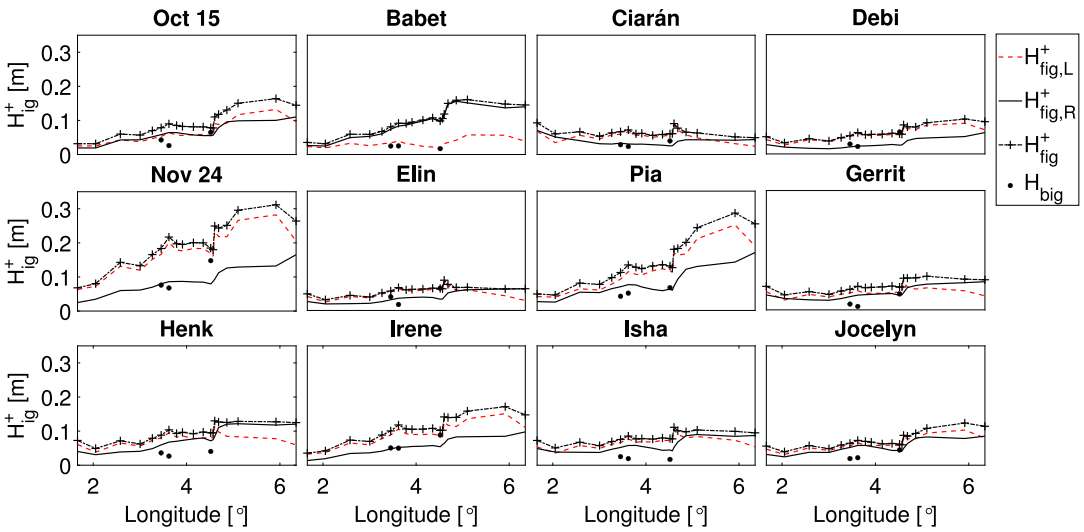

Fig. 10. H_{ig}^{+} of the different IG wave components (i.e., $H_{fig,L}^{+}$, $H_{fig,R}^{+}$, H_{fig}^{+} and H_{big}) as a function of longitude for twelve different storms that occurred during SP23/24. The BIG wave values (shown in black dots) are provided from left to right by OS11, BG2, and SPY.

domain. However, the impact of this shift is expected to be minimal, as the displacement is small (given as 2.083 km, see also detailed specifications of the modelled OS11 station in the Supplementary document). An additional factor which may result in the model underprediction of high H_{fig} values at OS11 is the underprediction of high H_{ss} by WW3 which is observed at station K13 (see Fig. 3) and at the nearshore stations OS11, BG2, REF and SPY (see Supplementary document, Figs. 1 and 2). Since the WW3 outputs are used here to force the seaward radiation of FIG waves, it is expected that the underprediction of WW3 will lead to a similar underprediction of the H_{fig} peaks. This may also explain the underprediction of H_{fig} peaks observed at station SPY and at some of the offshore stations. Finally, another factor that may explain the model underestimation of high H_{fig} values is the release of BIG waves due to sea-swell wave breaking or due to rapid bathymetry changes. This phenomenon gives rise to FIG energy that cannot be predicted based on the present model formulation.

At the offshore stations, the model accuracy tend to be less favourable compared to the accuracy at the nearshore stations (compare the MAE values presented in Figs. 8 and 9, and refer to Table 4 in Appendix A). Specifically, it seems that the MAE of the offshore stations is largely determined by deviations which consistently arise during periods of low H_{fig} values. This observation is most strikingly illustrated by stations K13 and J6 which also demonstrate the highest MAE values. In contrast, during periods of high H_{fig} values, the deviations at the offshore stations are less prominent (as also demonstrated by the model performance metrics given in Table 4). Interestingly, the offshore MAE values appear to be very close to the b values of the FIG fit shown by Fig. 4. This observation provides a strong indication that the source leading to the departure of b from zero (may be physical or limited measuring capabilities) is in fact the same source that gives rise to these less favourable MAE values offshore.

In summary, based on the verification examples and despite of the model deviations which particularly arise during periods of low H_{fig} values at the offshore stations, it can be said that the model is in good agreement with the available field observations (see also model agreement with observations of the characterized IG period and frequency distribution in the Supplementary document). The obtained model performance allows to expand the examination initiated in Section 3 and to evaluate in a reliable and more conclusive manner the importance of the shoreward propagating FIG waves and to gain insight into the contribution of FIG_R waves nearshore.

5. The importance of shoreward propagating FIG waves

The importance of the shoreward propagating FIG waves is studied here along the coasts of Belgium and the Netherlands at nearshore points aiming to represent offshore boundary conditions for nearshore process-based models. To this end, 19 points along the Belgium and the Netherlands coasts are considered over which the water depth is ranging from about 10 m to about 20 m, with an average of about 14 m (detailed specification of the water depths and coordinates of the points is given in Section 5 of the Supplementary document). The shoreward propagating FIG energy is evaluated at the considered nearshore points using the newly developed SWAN model. These points also include the nearshore stations OS11, BG2, REF, and SPY, where BIG energy data is available.

The analysis at the considered points distinguishes between three different energy contributions. These are the shoreward propagating energy of FIG_L waves, $E_{fig,L}^{+}$ (defined for the present discussion as contributions arriving from the BE and NL coasts), the shoreward propagating energy of FIG_R waves, $E_{fig,R}^{+}$ (defined as contributions arriving from the coasts of UK, GER, DK and NOR) and the energy due to BIG waves, E_{big}. An additional definition is the total shoreward propagating FIG energy, E_{fig}^{+}, defined as the sum of $E_{fig,L}^{+}$ and $E_{fig,R}^{+}$. Note that this distinction between local and remote FIG wave contributions is defined here to conveniently examine the sources of FIG generation. More strictly, $E_{fig,L}^{+}$ may be defined as the fraction of energy that can be determined exclusively by the sea-swell conditions at the nearshore point of interest. The source of this energy contribution is likely to be a narrow coastal zone surrounding the point of interest, which depends on the considered storm characteristics and the morphological characteristics at that point.

The predictions of $E_{fig,L}^{+}$ and $E_{fig,R}^{+}$ at each of the considered nearshore points are obtained through SWAN by activating only the local source lines (i.e., the lines specified along the BE and NL coasts) or only the remote source lines (i.e., the lines specified along the coasts of UK, GER, DK and NOR), respectively. After separately collecting local and remote energy contributions, the results are integrated in the frequency and direction spaces, where the integration in the direction space is performed with respect to the shore-normal direction at each point such that only shoreward propagating energy contributions are taken into account in the integration.

The results presented here are divided into storm dependent results (see Figs. 10–12) and results which present typical values under storm conditions (see Fig. 13). All of these results are based on measured and modelled data obtained for the storm periods SP22 and

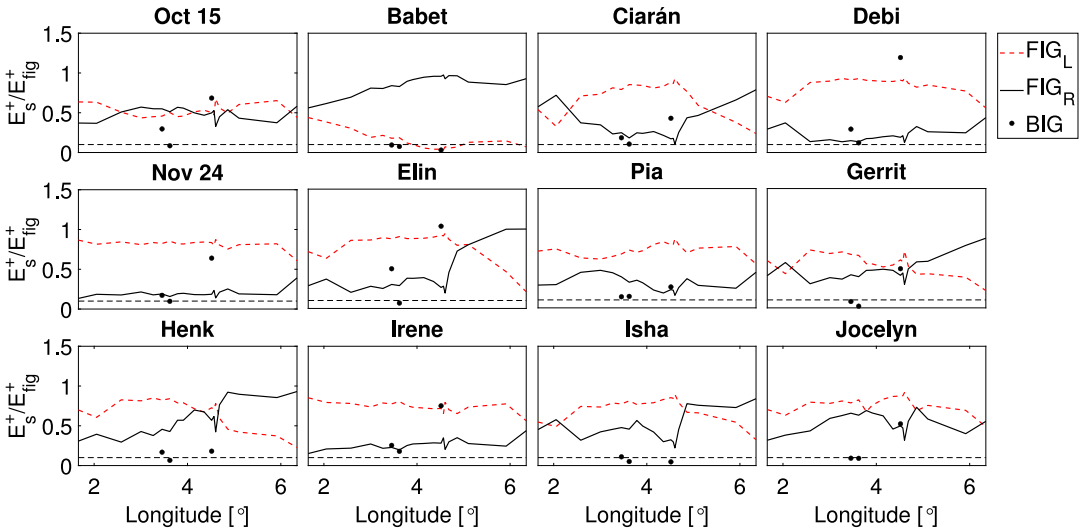

Fig. 11. The ratio between the maximum energy E_s^+ of the different IG wave components (i.e., FIG_L, FIG_R and BIG) and the maximum E_{fig}^+ as a function of longitude for twelve different storms that occurred during SP23/24. The BIG wave values (shown in black dots) are provided from left to right by OS11, BG2, and SPY. The dashed black lines indicate a ratio of 0.1.

SP23/24. The storm dependent results of Fig. 10 compare the maximum significant-wave-height values (H_{ig}^+) occurred during the different storms of SP23/24. The results show that H_{fig}^+ is higher than H_{big} at the measurement locations for almost all of the storms of SP23/24. Additionally, the incident IG heights are higher over the eastern points, where H_{fig}^+ reaches values of about 0.3 m in front of the coasts of the Dutch Wadden sea (at around Lon= 5°). By examining the different free components, it is shown that the values of $H_{fig,R}^+$ are generally comparable to those of H_{big} and typically lower than those of $H_{fig,L}^+$. However, there are storms leading to different conclusions, namely Oct 15, Babet, Henk, Isha and Joscelyn, for which $H_{fig,R}^+$ is equivalent and may even be significantly higher than $H_{fig,L}^+$.

The importance of the shoreward propagating FIG energy is also expressed through Fig. 11, which presents the maximum values of the energy components $E_{fig,L}^+$, $E_{fig,R}^+$ and E_{big} relative to the maximum value of E_{fig}^+ occurred during the different storms of SP23/24. The results show that for most of the storms E_{big} is smaller than about a half of E_{fig}^+ at all the measurement stations, while for some storms this ratio can be higher at station SPY. Moreover it is shown that for most of the storms, E_{big} at the western stations (OS11 and BG2) demonstrates only a negligible contribution (of about 0.1, see the dashed black line in Fig. 11) relative to the contribution of E_{fig}^+. Fig. 11 also shows that the contribution of $E_{fig,L}^+$ is often the dominant IG energy component nearshore. However, there are storms for which $E_{fig,R}^+$ dominates especially at the eastern points (see storms Babet, Ciarán, Elin, Gerrit, Henk and Isha) and storms for which $E_{fig,L}^+$ and E_{big} show significantly lower values comparing to $E_{fig,R}^+$ (see storms Babet and Henk). The example of storm Babet is particularly noteworthy because of its unique storm conditions that led to significant H_{ig}^+ values along the BE and NL coasts (see Fig. 10) that are almost entirely explained by the contribution of $E_{fig,R}^+$. This example clearly emphasizes that generally the incoming FIG wave conditions nearshore at a particular coast in the North Sea cannot be determined exclusively by the local sea-swell conditions, but require a broader domain that depends on the location of the coast and the track of the storm.

The dependence of the nearshore IG conditions on the storm is examined in further detail through Fig. 12. This figure show similar results to those of Fig. 11, however here, the contributions of remote sources are presented separately. The presented results are the energy ratios of three storms occurred during SP22 (see the upper panels of Fig. 12) and the energy ratios of three storms occurred during SP23/24 (see the lower panels of Fig. 12). These storms are the ones for which the spatial distribution of the horizontal wind field at the storm peaks is plotted in Fig. 7. Examination of both Figs. 7 and 12 clarifies the relation between the coastal regions to which the wind is blowing at the storm peak and the degree of importance of the various IG energy sources (as also observed by Rijnsdorp et al., 2021). These results show how storms that are characterized by a significant westerly wind component (e.g., Corrie (a) and Pia) involve relatively important FIG energy contributions originating from GER, DK and NOR. Whereas, storms that are characterized by a significant northerly wind component (e.g., Jan 20, Corrie (b) and Nov 24) leading to significant local FIG and BIG energy contributions. At the peak of storm Babet, however, an easterly wind component dominated and in addition the magnitude of the wind velocity along the BE and most of NL coasts was relatively weak (see Fig. 7). These conditions led to the fact that the nearshore IG wave conditions along the coasts of BE and NL were dominated by energy originating from the coasts of UK, while local IG energy (i.e., $E_{fig,L}^+$ and E_{big}) was negligible. These results support the explanation assumed in Section 3 that the high energy ratio between E_{fig} and E_{big} observed at the nearshore measuring stations during Storm Babet (see Fig. 6) is due to FIG energy originating from the coasts of UK.

A more general perspective on the importance of shoreward propagating FIG waves along the BE and NL coasts is shown by the results of Fig. 13. These results aim to describe the importance of shoreward propagating FIG waves under general storm conditions without distinguishing between different storms. To this end, the typical relative energy contributions of BIG and FIG waves are examined as functions of the longitudinal position and the sea-swell wave height (i.e., H_{ss}). The typical energy ratios depicted in Fig. 13 are found based on the different energy values (i.e., $E_{fig,L}^+$, $E_{fig,R}^+$ and E_{big}) obtained simultaneously under storm conditions, i.e. at times when $H_{fig} > 0.1$ m during SP22 and SP23/24. The upper panel of Fig. 13 shows that the typical relative contribution (defined through the median) of $E_{fig,L}^+$ is higher than that of $E_{fig,R}^+$ and E_{big}. In addition, it also suggests that the typical contribution of E_{big} can vary dramatically in space, from values of about 5–10% of E_{fig}^+ at the western stations (i.e., OS11 and BG2) to about 30–50% of E_{fig}^+ at the eastern stations (i.e., REF and SPY). Finally, note that this panel points to an artifact of the distinction defined here between remote and local FIG energy contributions. This artifact is explained based on the two easternmost nearshore points. These points are subject to similar depth and sea-swell conditions, yet exhibit significantly different energy ratios. The apparent decrease in $E_{fig,L}^+$

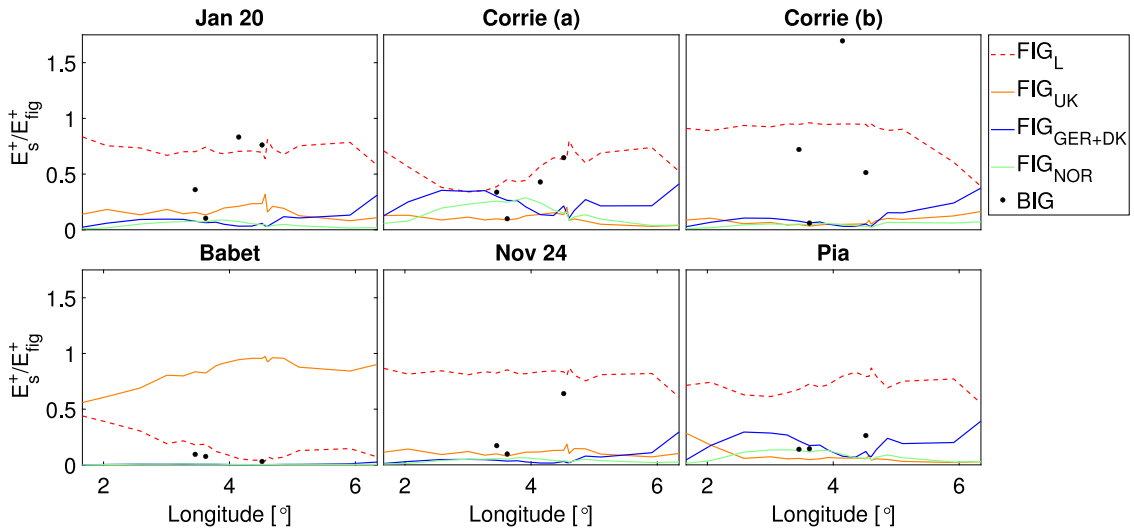

Fig. 12. The ratio between the maximum energy E_s^+ of the different IG wave components (i.e., FIG$_L$, FIG$_{UK}$, FIG$_{GER+DK}$, FIG$_{NOR}$ and BIG) and the maximum E_{fig}^+ as a function of longitude for three storms occurred during SP22 (upper panels) and three storms occurred during SP23/24 (lower panels). Where, FIG$_{UK}$, FIG$_{GER+DK}$ and FIG$_{NOR}$ waves are FIG waves originating from UK coasts, the coasts of GER and DK and the coasts of NOR respectively. In the upper panels, the BIG wave values (shown in black dots) are provided from left to right by OS11, BG2, REF and SPY. In the lower panels, the BIG wave values are provided from left to right by OS11, BG2, and SPY.

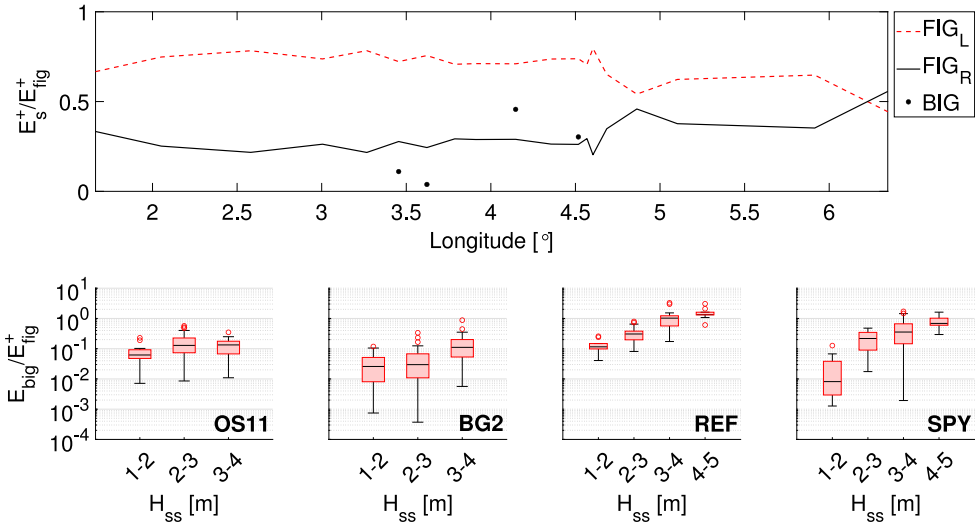

Fig. 13. The spatial dependent median (upper panel) and H_{ss} dependent box plots (lower panels) of different energy ratios under storm conditions, i.e. at times when $H_{fig} > 0.1$ m. In the upper panel, the BIG wave values (shown in black dots) are provided from left to right by OS11, BG2, REF and SPY.

and increase in $E_{fig,R}^+$ at the easternmost point may be attributed to the absence of local eastern energy sources, as this point lies at the edge of the NL source line. This also suggests that in this region, the typical alongshore extent responsible for most of the locally generated FIG energy is less than twice the distance between these two easternmost points, i.e., less than about 1° (approximately 66 km at this latitude).

The lower panels provide additional details on the typical ratio between E_{big} and E_{fig}^+ at the locations of the measurement stations. Specifically, it is shown how this ratio is distributed (through the use of box plots) for different ranges of H_{ss}. In general, it is shown that the typical relative contribution of E_{big} tends to be higher for higher H_{ss} values. Furthermore, similar to the observation made for the upper panel, also the lower panels suggest that the typical contributions of E_{big} at the western points are significantly lower than those at the eastern points. This spatial dependence also holds for the range of the highest H_{ss} values. Relative to E_{fig}^+, the contribution of E_{big} for these highest H_{ss} values is mainly populated in the percentage range 5–20% for OS11 and BG2, 130–162% for REF, and 50–102% for SPY. These results provide some insight into the FIG energy values to be considered nearshore along the BE and NL coasts in terms of energy ratio with E_{big} (where the latter can be estimated based on the local sea-swell wave conditions) and emphasize the importance of shoreward propagating FIG energy especially for nearshore western points.

In summary, it is observed that the importance of E_{fig}^+ is strongly spatially dependent. Relative to E_{big}, the contribution of E_{fig}^+ significantly dominates at OS11 and BG2 and often dominates at REF and SPY as well. In addition, E_{fig}^+ and its components (i.e., $E_{fig,L}^+$ and $E_{fig,R}^+$) are observed to depend on the type of storm. Where, E_{fig}^+ is mostly dominated by $E_{fig,L}^+$, especially for storms characterized by a significant northerly wind component. However, storm cases for which E_{fig}^+ is dominated by $E_{fig,R}^+$ are also presented here, especially over the western points and for storms characterized by a significant westerly or easterly wind component. These cases emphasize the need to account for remote FIG energy contributions to properly define the IG wave conditions nearshore along the BE and NL coasts. Finally, based on the

results and observations gathered here, it is expected that the neglect of FIG energy contributions, as implemented by current design practice, can potently lead to underestimation of the coastal impacts associated with IG waves.

6. Discussion

6.1. Nearshore FIG conditions for coastal safety assessment

The nearshore design conditions of IG waves are required for coastal safety assessments. Through the processed-based approach, these design conditions are used to force small-scale models (e.g., XBeach, Roelvink et al., 2009 and SWASH, Zijlema et al., 2011) which can accurately estimate flood risk parameters such as wave runup and overtopping. Based on the design conditions of the sea-swell waves, the nearshore BIG energy is determined directly through second-order theory (Hasselmann, 1962). However, as demonstrated in Section 5, the nearshore FIG energy contribution along the North Sea coasts is not easily evaluated, because it cannot be determined exclusively by local sea-swell conditions and because of its strong dependence on the characteristics of the storm considered. This suggests that the design FIG conditions may be obtained under certain storm characteristics, which are not necessarily considered for the determination of the design sea-swell conditions. To demonstrate this suggestion, consider for example the wave conditions obtained at the nearshore station SPY during the two significant storms Corrie (b) and Nov 24. Interestingly, both of these storms led to similar sea-swell conditions (with $H_{ss} \approx 5$ m and $T_{m-10} \approx 10$ s), but resulted in different FIG responses. Specifically, the maximum H_{fig} obtained during Nov 24 was almost 10 cm higher than the maximum H_{fig} obtained during Corrie (b) (see H_{fig} observations in Figs. 8–9). This difference may be explained by the alongshore pattern of the wind fields at the storm peak, as described in Fig. 7. The figure shows that the coastal area subject to strong winds around SPY was much larger at the peak of storm Nov 24 than at the peak of storm Corrie (b). Therefore, besides the local FIG response, which might be similar based on the sea-swell conditions, stronger contributions from, e.g., the Belgian coasts or the eastern Dutch coasts were likely to occur during Nov 24 and led to the higher H_{fig} result. Therefore, the nearshore FIG conditions is not only dependent on the local wind speeds and the corresponding local sea-swell conditions, but also on the alongshore pattern of the wind fields associated with the considered storm.

Based on the results of Section 5, another storm factor which may influence the nearshore FIG conditions is the storm track. Investigation of this factor, for a particular nearshore point in the North Sea, should consider long-term historical data of storm evolution and possible storm behaviour changes in the North Sea (e.g., De Winter et al., 2013) to determine possible storm track scenarios and the storm path leading to the most hazardous combination of sea-swell and IG wave conditions. While this study is confined to specific storm periods, it is plausible that certain storm scenarios (although their probability is unknown) could lead to even more intense FIG conditions than those observed. For example, the period between the peak of storms Corrie (a) and Corrie (b), which lasted more than a day, could have been shorter, such that the FIG waves radiated from DK and GER due to Corrie (a) would coincide with the locally generated FIG due to Corrie (b) along the BE and NL coasts. Another intense scenario could have occurred if storm Babet had turned southwards instead of northwards (the northwards propagation is shown by ERA5 hindcasts, see Hersbach et al., 2023) at such a pace that it would have led to interference of FIG waves radiated from UK and FIG waves generated locally along the BE and NL coasts. These descriptive scenarios aim to highlight the potential uncertainty inherent in FIG conditions during storms and to emphasize the fact that in addition to wind speeds and alongshore wind pattern, the design FIG conditions should also consider the storm track. Ultimately, given a design storm for a certain coastal location in the North Sea, the corresponding FIG conditions can be estimated based on the unstructured SWAN model developed in this study.

6.2. Estimated mapping of FIG and BIG energy ratios between nearshore and breaking points

Section 5 examined the importance of shoreward propagating FIG energy at the offshore boundaries along the BE and NL coasts. However, the fact that throughout the shoaling process the BIG energy density increases faster than the FIG energy density, raises doubt concerning the actual relative contribution of the latter at the shoreline. This is tested here under the assumption that beyond the sea-swell breakpoint, the energy densities considered as bound or free at the nearshore points would amplified equivalently up to the shoreline (as demonstrated, e.g., by Ruessink et al., 2013). Thus, the considered mapping is between the energy ratios of BIG and FIG waves at the nearshore point and the ratios at the sea-swell breakpoint. Mathematically, this mapping can be written using the following parameterization:

$$\left(\frac{E_{big}}{E^{+}_{fig}}\right)_{h=h_{br}} = \left(\frac{E_{big}}{E^{+}_{fig}}\right)_{h=h_{nr}} \left(\frac{h_{nr}}{h_{br}}\right)^{\alpha_{big}-\alpha_{fig}} \tag{17}$$

where h_{nr} and h_{br} are the water depths at the nearshore point (say at one of the 19 points analysed in Section 5) and at the breakpoint, respectively. Additionally, α_{fig} and α_{big} represent the amplification factors of the BIG and shoreward propagating FIG energy densities.

Based on the mapping defined in (17), the upper panels of Fig. 14 estimate the energy ratio E_{big}/E^{+}_{fig} at the shorelines in front of OS11, BG2, REF and SPY for different combinations of α_{fig} and α_{big}. The value range for α_{fig} is determined to be between the value of Green's Law (i.e., $\alpha_{fig} = 0.5$) and the value that corresponds to refractively trapped FIG waves (i.e., $\alpha_{fig} = 1$, following Herbers et al., 1995b) under the assumption that E^{+}_{fig} consists of the contribution of both locally trapped and remotely generated FIG waves. The values of α_{big} can range rather significantly according to the normalized bed slope parameter (e.g., Battjes et al., 2004; Van Dongeren et al., 2007; Zhang et al., 2020) and other factors such as the directional spreading (e.g., Herbers and Burton, 1997). Here, the minimum value for α_{big} is chosen so that it is not lower than α_{fig} (i.e., $\alpha_{big} = 1$) and not higher than the equilibrium solution of Longuet-Higgins and Stewart (1962) (i.e., $\alpha_{big} = 5$). Furthermore, the mapping of (17) also requires to evaluate the nearshore ratio $(E_{big}/E^{+}_{fig})_{h=h_{nr}}$, the breakpoint depth h_{br} and the nearshore depth h_{nr}. The latter is detailed for the considered stations in Table 1 and the former is assumed based on the considered incoming H_{ss} range and according to the median values detailed by the lower panels of Fig. 13. Additionally, the breakpoint depth is determined through the relation $h_{br} = H_{ss}/\gamma_{br}$ and under the assumption that $\gamma_{br} \approx 0.5$. The results of the upper panels are obtained assuming incoming sea-swell height range of $H_{ss} \in [3, 4]$ m, which is the highest range observed at OS11 and BG2. According to the midpoints of the panels (see the black dots at the centre of the panels), which show the results for $\alpha_{fig} = 0.75$ and $\alpha_{big} = 3$, the shoreline energy ratios are about 2–4 at REF and SPY and about 0.2–0.25 at OS11 and BG2. In terms of wave heights, these results suggest an increase of 10–20% and 225–250% of the incoming IG wave heights due to the contribution of the incoming FIG energy at the eastern stations (i.e. REF and SPY) and western stations (i.e. OS11 and BG2), respectively. Further insights are gained through the results of the lower panel. Specifically, this panel illustrates how the shoreline energy ratio depends on the incoming sea-swell wave conditions by showing the cross-shore evolution of the energy ratio in front of REF for two different ranges of H_{ss}. This dependence is characterized by two opposing effects. On one hand, as H_{ss} increases, the breakpoint shifts further offshore. This results in a narrower shoaling region, where the energy density of the BIG waves typically amplifies faster than the energy density of the FIG waves. As demonstrated by the lower panel, this effect increases the dominance of incoming FIG energy at the breakpoint and at the shoreline. On the other hand, values of $(E_{big}/E^{+}_{fig})_{h=h_{nr}}$ also tend to increase with higher H_{ss} (see also the lower panels of Fig. 13). This trend enhances the relative contribution of BIG energy at the breakpoint and shoreline.

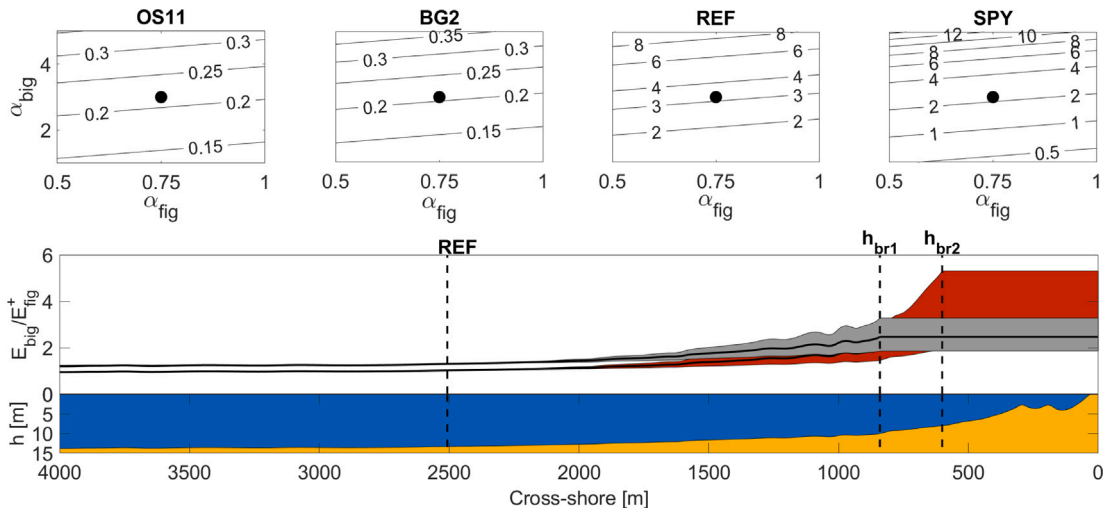

Fig. 14. Upper panels: Estimated energy ratios (E_{big}/E^{+}_{fig}) at the shorelines in front of OS11, BG2, REF and SPY for different combinations of α_{fig} and α_{big}, assuming incoming sea-swell wave heights of $H_{ss} \in [3,4]$ m and corresponding breakpoint depth of $h_{br} = 8$ m. Lower panel: Cross-shore evolution of the energy ratio from the nearshore station REF to the shoreline assuming $\alpha_{fig} = 0.75$ and the range $\alpha_{big} \in [2,4]$ for two different incoming sea-swell conditions and corresponding breakpoints, i.e. $H_{ss} \in [4,5]$ m with assumed $h_{br1} = 10$ m (gray fill) and $H_{ss} \in [3,4]$ m with assumed $h_{br2} = 8$ m (red fill). Additionally the cross-shore bottom profile is obtained from Rutten et al. (2024) and illustrated by the yellow fill. Finally, the three vertical dashed lines indicate from left to right the cross-shore location of station REF, h_{br1} and h_{br2}.

In summary, this analysis suggests that the important contribution of FIG energy may extend further shoreward, beyond the offshore boundaries, potentially reaching all the way to the shoreline. Specifically, it is suggested that along the Dutch coasts, the shoreward propagating FIG energy at the shoreline could be comparable to, or even exceed, the contribution due to BIG energy, particularly under conditions of high sea-swell waves for which the breakpoint shifts significantly offshore and along the western Dutch coasts (i.e., the coasts of Zeeland). Finally, it is important to note that the analysis presented here relies on simplified assumptions and arguments, which introduce uncertainty into its quantitative estimates. The highlighted potential importance of FIG energy along shorelines emphasizes the need for a more accurate investigation of cross-shore IG wave evolution (e.g., using detailed modelling tools such as XBeach, Roelvink et al., 2009 or SWASH, Zijlema et al., 2011).

7. Conclusions

This study develops an unstructured SWAN model for the prediction of FIG waves in the North Sea. The model is verified based on a new collection of offshore and nearshore observations of IG waves over the southern North Sea. Good agreement is found between the modelled and observed results for two recent storm periods (during the winter of 2022 and the fall/winter of 2023/24). The model shows relatively low mean absolute error (MAE) nearshore and somewhat higher MAE values offshore. Offshore MAE values are governed by discrepancies that occur during calm sea-swell conditions. This is consistent with radar-based observations, demonstrating residual FIG heights for very low sea-swell heights, which could not be explained by the model and may related to measurement error or unidentified physical phenomenon. Accordingly and also due to the fact that the model is strongly dependent on calibration data, significant model improvement may be achieved by collecting and validating existing measurement data and by implementing advanced measurement capabilities (e.g., Rutten et al., 2024; Nose et al., 2024) and new data processing methods (e.g., Matsuba et al., 2022).

Based on the modelled and measured observations, the study also demonstrates the importance of shoreward propagating FIG energy at nearshore locations along the coasts of Belgium and the Netherlands. The sources and intensity of shoreward propagating FIG energy are found to be strongly dependent on the storm characteristics (i.e., alongshore wind pattern and the trajectory of the storm). Additionally, the significant FIG energy obtained from remote sources during certain storm scenarios (e.g., storm Babet) suggests the inherent potential for amplified FIG conditions nearshore as a result of possible interference between locally and remotely generated FIG waves. These insights lead to the conclusion that in addition to wind speeds, the definition for the design conditions for FIG waves nearshore must also account for the alongshore wind pattern and storm track. Ultimately, comparison of the energy ratios of FIG and BIG waves as obtained at nearshore locations and as evaluated at the shoreline, indicates the importance of considering the FIG as an integral part of coastal safety assessments along the coasts of the North Sea.

CRediT authorship contribution statement

Gal Akrish: Writing – original draft, Validation, Software, Methodology, Investigation, Formal analysis, Conceptualization. **Ad Reniers:** Writing – review & editing, Supervision, Resources, Methodology, Data curation, Conceptualization. **Dirk Rijnsdorp:** Writing – review & editing, Supervision, Methodology, Conceptualization. **Marcel Zijlema:** Writing – review & editing, Validation, Supervision, Software, Methodology. **Jantien Rutten:** Writing – review & editing, Supervision, Investigation, Data curation. **Marion Tissier:** Writing – review & editing, Supervision.

Declaration of competing interest

The authors declare that they have no known competing financial interests or personal relationships that could have appeared to influence the work reported in this paper.

Acknowledgements

This research is part of the “Kennis voor Keringen”, research for flood defenses program of Rijkswaterstaat, part of the Dutch Ministry of Infrastructure and Water Management. The authors thank Robert Slomp and Robert Vos for supporting this research, and Pieter Dekker for his help with processing the sea surface data. The authors also thank Marcel Bottema, Jacco Groeneweg and Joana van Nieuwkoop for their insightful suggestions that helped improve this paper.

Table 4
Model performance metrics at the different stations during SP22 and SP23/24 (the metrics for the two storm periods are separated by '/').

Station	General conditions			Storm conditions ($H_{fig} > 0.1$ m)		
	MAE [cm]	CL [%]	MP [%]	MAE [cm]	CL [%]	MP [%]
OS11	1.55/1.16	90/89	75/77	5.01/3.35	91/91	73/80
BG2	1.17/1.20	86/87	70/72	2.78/2.27	87/92	82/84
EUR	–/2.06	–/99	–/59	–/2.05	–/93	–/83
REF	1.70/–	89/–	49/–	2.87/–	82/–	80/–
SPY	1.26/1.45	93/93	75/73	2.29/2.45	86/85	85/83
K13	3.24/3.94	98/100	59/50	3.71/2.96	94/91	70/75
J6	–/3.82	–/99	–/51	–/3.41	–/92	–/71
D15	–/2.29	–/93	–/64	–/4.85	–/92	–/65
F3	–/2.69	–/95	–/62	–/3.49	–/88	–/73
A12	1.94/–	91/–	74/–	3.55/–	87/–	74/–

Appendix A. Model performance

The MAE is largely influenced by errors during calm conditions, where H_{fig} is relatively low and errors are expected to be small. This raises questions about how representative the MAE is for all error values. The dominance of low errors during calm periods also limits the MAE to provide assessment of model performance. This difficulty applies to both calm and storm conditions. Here, these concerns are addressed by introducing additional metrics to evaluate the representativeness of the MAE and the predictive capability of the model under both general and storm conditions.

To gain insight into the ability of MAE to represent the errors made by the model, the following confidence level (CL) measure is define:

$$CL = \frac{\text{Number of errors smaller than } 2 \times \text{MAE}}{\text{Total number of errors}} \times 100 \tag{18}$$

In addition, the capability of the model to predict the observed H_{fig} values is assessed by examining the MAE relative to the averaged value of the observed H_{fig}, defined as $\langle H_{fig}^{obs} \rangle$. Accordingly, the following model performance (MP) measure is introduced:

$$MP = \left(1 - \frac{\text{MAE}}{\langle H_{fig}^{obs} \rangle}\right) \times 100 \tag{19}$$

Finally, note that the MP measure is closely related to the model skill parameter (Gallagher et al., 1998), except that the former is based on the mean absolute values.

Table 4 presents a summary of the metrics obtained at the different stations during SP22, SP23/24, and under general and storm conditions. General conditions refer to all times, whereas storm conditions refer to times when the observed H_{fig} exceeds 0.1 m.

The CL values suggest that the model error mostly remains close to the MAE, indicating consistent model prediction across all stations. This consistency is also evident by comparing the MP values for the general and storm conditions. When calm conditions are significant (refer to the metrics for general conditions), the MP values at stations showing consistent underprediction (e.g., K13, J6) or overprediction (e.g., REF) (see Figs. 8–9) indicate relatively poor model performance. However, this performance improves significantly under storm conditions (e.g, MP at REF increases by 31% during SP22, and MP at K13 increases by 25% during SP23/24), for which the calm conditions are excluded.

Appendix B. Supplementary data

Supplementary material related to this article can be found online at https://doi.org/10.1016/j.ocemod.2025.102619.

Data availability

Links to download or request the data used in this study are provided in a separate attached file.

Mean sea level bathymetry (Reference data)
Measurement data (Reference data)
Data collected at station REF (Reference data)
Sea-swell data (Reference data)
ERA5 hourly wind data (Reference data)

References

Ardhuin, F., Rawat, A., Aucan, J., 2014. A numerical model for free infragravity waves: Definition and validation at regional and global scales. Ocean. Model. 77, 20–32.

Athanasiou, P., Van Dongeren, A., Giardino, A., Vousdoukas, M., Gaytan-Aguilar, S., Ranasinghe, R., 2019. Global distribution of nearshore slopes with implications for coastal retreat. Earth Syst. Sci. Data 11 (4), 1515–1529.

Barnard, P.L., van Ormondt, M., Erikson, L.H., Eshleman, J., Hapke, C., Ruggiero, P., Adams, P.N., Foxgrover, A.C., 2014. Development of the coastal storm modeling system (CoSMoS) for predicting the impact of storms on high-energy, active-margin coasts. Nat. Hazards 74, 1095–1125.

Battjes, J., Bakkenes, H., Janssen, T., van Dongeren, A.R., 2004. Shoaling of subharmonic gravity waves. J. Geophys. Res.: Ocean. 109 (C2).

Baumann, J., Chaumillon, E., Bertin, X., Schneider, J.-L., Guillot, B., Schmutz, M., 2017. Importance of infragravity waves for the generation of washover deposits. Mar. Geol. 391, 20–35.

Bertin, X., de Bakker, A., van Dongeren, A., Coco, G., André, G., Ardhuin, F., Bonneton, P., Bouchette, F., Castelle, B., Crawford, W.C., Davidson, M., Deen, M., Dodet, G., Guérin, T., Inch, K., Leckler, F., McCall, R., Muller, H., Olabarrieta, M., Roelvink, D., Ruessink, G., Sous, D., Stutzmann, É., Tissier, M., 2018. Infragravity waves: From driving mechanisms to impacts. Earth-Sci. Rev. 177, 774–799.

Booij, N., Ris, R.C., Holthuijsen, L.H., 1999. A third-generation wave model for coastal regions: 1. Model description and validation. J. Geophys. Res.: Ocean. 104 (C4), 7649–7666.

Cheriton, O.M., Storlazzi, C.D., Rosenberger, K.J., 2016. Observations of wave transformation over a fringing coral reef and the importance of low-frequency waves and offshore water levels to runup, overwash, and coastal flooding. J. Geophys. Res.: Ocean. 121 (5), 3121–3140.

Crawford, W., Ballu, V., Bertin, X., Karpytchev, M., 2015. The sources of deep ocean infragravity waves observed in the North Atlantic Ocean. J. Geophys. Res.: Ocean. 120 (7), 5120–5133.

De Winter, R., Sterl, A., Ruessink, B., 2013. Wind extremes in the North Sea Basin under climate change: An ensemble study of 12 CMIP5 GCMs. J. Geophys. Res.: Atmos. 118 (4), 1601–1612.

Dodet, G., Melet, A., Ardhuin, F., Bertin, X., Idier, D., Almar, R., 2019. The contribution of wind-generated waves to coastal sea-level changes. Surv. Geophys. 40 (6), 1563–1601.

Elgar, S., Herbers, T., Okihiro, M., Oltman-Shay, J., Guza, R., 1992. Observations of infragravity waves. J. Geophys. Res.: Ocean. 97 (C10), 15573–15577.

Emanuel, K.A., 2013. Downscaling CMIP5 climate models shows increased tropical cyclone activity over the 21st century. Proc. Natl. Acad. Sci. 110 (30), 12219–12224.

Ewans, K., Feld, G., Jonathan, P., 2014. On wave radar measurement. Ocean. Dyn. 64 (9), 1281–1303.

Fa, C., 2021. Infragravity Waves on the North Sea: Generation, Propagation and Dissipation Mechanisms (M.Sc. Thesis). Delft University of Technology.

Fiedler, J.W., Smit, P.B., Brodie, K.L., McNinch, J., 2019. The offshore boundary condition in surf zone modeling. Coast. Eng. 143, 12–20.

Gallagher, E.L., Elgar, S., Guza, R., 1998. Observations of sand bar evolution on a natural beach. J. Geophys. Res.: Ocean. 103 (C2), 3203–3215.

Godin, O.A., Zabotin, N.A., Sheehan, A.F., Yang, Z., Collins, J.A., 2013. Power spectra of infragravity waves in a deep ocean. Geophys. Res. Lett. 40 (10), 2159–2165.

Guza, R.T., Thornton, E.B., 1982. Swash oscillations on a natural beach. J. Geophys. Res.: Ocean. 87 (C1), 483–491.

Hasselmann, K., 1962. On the non-linear energy transfer in a gravity-wave spectrum Part 1. General theory. J. Fluid Mech. 12 (4), 481–500.

Hasselmann, K., Barnett, T.P., Bouws, E., Carlson, H., Cartwright, D.E., Enke, K., Ewing, J., Gienapp, A., Hasselmann, D., Kruseman, P., et al., 1973. Measurements of wind-wave growth and swell decay during the Joint North Sea Wave Project (JONSWAP).. Ergaenzungsheft Dtsch. Hydrogr. Z. Reihe A.

Herbers, T., Burton, M., 1997. Nonlinear shoaling of directionally spread waves on a beach. J. Geophys. Res.: Ocean. 102 (C9), 21101–21114.

Herbers, T., Elgar, S., Guza, R., 1994. Infragravity-frequency (0.005–0.05 Hz) motions on the shelf. Part I: Forced waves. J. Phys. Oceanogr. 24 (5), 917–927.

Herbers, T., Elgar, S., Guza, R., 1995a. Generation and propagation of infragravity waves. J. Geophys. Res.: Ocean. 100 (C12), 24863–24872.

Herbers, T., Elgar, S., Guza, R., O'Reilly, W., 1995b. Infragravity-frequency (0.005–0.05 hz) motions on the shelf. Part II: Free waves. J. Phys. Oceanogr. 25 (6), 1063–1079.

Hersbach, H., Bell, B., Berrisford, P., Biavati, G., Horányi, A., Muñoz Sabater, J., Nicolas, J., Peubey, C., Radu, R., Rozum, I., Schepers, D., Simmons, A., Soci, C., Dee, D., Thépaut, J.-N., 2023. ERA5 hourly data on single levels from 1940 to present. Copernic. Clim. Chang. Serv. (C3S) Clim. Data Store (CDS).

Jangir, P.K., Ewans, K.C., Young, I.R., 2022. On the functionality of radar and laser ocean wave sensors. J. Mar. Sci. Eng. 10 (9), 1260.
Longuet-Higgins, M.S., Stewart, R., 1962. Radiation stress and mass transport in gravity waves, with application to 'surf beats'. J. Fluid Mech. 13 (4), 481–504.
Matsuba, Y., Roelvink, D., Reniers, A.J., Rijnsdorp, D.P., Shimozono, T., 2022. Reconstruction of directional spectra of infragravity waves. J. Geophys. Res.: Ocean. 127 (7), e2021JC018273.
May, V.J., Hansom, J.D., 2003. Coastal geomorphology of great britain. In: Geological Conservation Review Series, No. 28. Joint Nature Conservation Committee, Peterborough.
McCall, R.T., De Vries, J.V.T., Plant, N., Van Dongeren, A., Roelvink, J., Thompson, D., Reniers, A., 2010. Two-dimensional time dependent hurricane overwash and erosion modeling at Santa Rosa Island. Coast. Eng. 57 (7), 668–683.
Neale, J., Harmon, N., Srokosz, M., 2015. Source regions and reflection of infragravity waves offshore of the U.S.s Pacific Northwest. J. Geophys. Res.: Ocean. 120 (9), 6474–6491.
Neumann, B., Vafeidis, A.T., Zimmermann, J., Nicholls, R.J., 2015. Future coastal population growth and exposure to sea-level rise and coastal flooding – A global assessment. PLoS One 10 (3), e0118571.
Nose, T., Babanin, A.V., Ewans, K., 2024. Directional characteristics of infragravity waves during storms in the Nearshore Coastal Region. J. Coast. Res. 40 (2), 353–363.
Oh, J.-E., Chang, Y.S., Ryu, K.H., Jeong, W.M., 2023. Infragravity wave height dependency on short wave parameters – observations on the east coast of South Korea. Front. Mar. Sci. 10, 1194472.
Okihiro, M., Guza, R., Seymour, R., 1992. Bound infragravity waves. J. Geophys. Res.: Ocean. 97 (C7), 11453–11469.
Rawat, A., Ardhuin, F., Ballu, V., Crawford, W., Corela, C., Aucan, J., 2014. Infragravity waves across the oceans. Geophys. Res. Lett. 41 (22), 7957–7963.
Reniers, A., Groenewegen, M., Ewans, K., Masterton, S., Stelling, G., Meek, J., 2010. Estimation of infragravity waves at intermediate water depth. Coast. Eng. 57 (1), 52–61.
Reniers, A.J., Naporowski, R., Tissier, M.F., de Schipper, M.A., Akrish, G., Rijnsdorp, D.P., 2021. North Sea infragravity wave observations. J. Mar. Sci. Eng. 9 (2), 141.
Rijnsdorp, D.P., Reniers, A.J., Zijlema, M., 2021. Free infragravity waves in the North Sea. J. Geophys. Res.: Ocean. 126 (8), e2021JC017368.
Roberts, K.J., Pringle, W.J., Westerink, J.J., 2019. OceanMesh2D 1.0: MATLAB-based software for two-dimensional unstructured mesh generation in coastal ocean modeling. Geosci. Model. Dev. 12 (5), 1847–1868.
Roeber, V., Bricker, J.D., 2015. Destructive tsunami-like wave generated by surf beat over a coral reef during Typhoon Haiyan. Nat. Commun. 6 (1), 7854.
Roelvink, D., Reniers, A., Van Dongeren, A., De Vries, J.V.T., McCall, R., Lescinski, J., 2009. Modelling storm impacts on beaches, dunes and barrier islands. Coast. Eng. 56 (11–12), 1133–1152.
Ruessink, B.G., Michallet, H., Bonneton, P., Mouazé, D., Lara, J.L., Silva, P.A., Wellens, P., 2013. GLOBEX: Wave dynamics on a gently sloping laboratory beach. In: 7th International Conference on Coastal Dynamics. pp. 1351–1362.
Ruggiero, P., Holman, R.A., Beach, R., 2004. Wave run-up on a high-energy dissipative beach. J. Geophys. Res.: Ocean. 109 (C6).
Rutten, J., Tissier, M., van Wiechen, P., Zhang, X., de Vries, S., Reniers, A., Mol, J.-W., 2024. Continuous wave measurements collected in intermediate depth throughout the North Sea storm season during the realdune/reflex experiments. Data 9 (5), 70.
Rutten, J., Torres-Freyermuth, A., Puleo, J., 2021. Uncertainty in runup predictions on natural beaches using XBeach nonhydrostatic. Coast. Eng. 166, 103869.
Smit, P., Janssen, T., Herbers, T., Taira, T., Romanowicz, B., 2018. Infragravity wave radiation across the shelf break. J. Geophys. Res.: Ocean. 123 (7), 4483–4490.
SWAN Team, 2024. SWAN Technical Documentation, SWAN Cycle III, Version 41.51. Delft University of Technology, Delft, The Netherlands.
Tolman, H.L., et al., 2009. User manual and system documentation of WAVEWATCH III TM version 3.14. Tech. Note MMAB Contrib. 276 (220).
Tonegawa, T., Fukao, Y., Shiobara, H., Sugioka, H., Ito, A., Yamashita, M., 2018. Excitation location and seasonal variation of transoceanic infragravity waves observed at an absolute pressure gauge array. J. Geophys. Res.: Ocean. 123 (1), 40–52.
Turner, I.L., Leaman, C.K., Harley, M.D., Thran, M.C., David, D.R., Splinter, K.D., Matheen, N., Hansen, J.E., Cuttler, M.V., Greenslade, D.J., Zieger, S., Lowe, R.J., 2024. A framework for national-scale coastal storm hazards early warning. Coast. Eng. 192, 104571.
Van Dongeren, A., Battjes, J., Janssen, T., Van Noorloos, J., Steenhauer, K., Steenbergen, G., Reniers, A., 2007. Shoaling and shoreline dissipation of low-frequency waves. J. Geophys. Res.: Ocean. 112 (C2).
Vousdoukas, M.I., Ferreira, Ó., Almeida, L.P., Pacheco, A., 2012. Toward reliable storm-hazard forecasts: Xbeach calibration and its potential application in an operational early-warning system. Ocean. Dyn. 62, 1001–1015.
Vrećica, T., Soffer, R., Toledo, Y., 2019. Infragravity wave generation by wind gusts. Geophys. Res. Lett. 46 (16), 9728–9738.
Webb, S.C., Zhang, X., Crawford, W., 1991. Infragravity waves in the deep ocean. J. Geophys. Res.: Ocean. 96 (C2), 2723–2736.
Winter, G., Storlazzi, C., Vitousek, S., Van Dongeren, A., McCall, R., Hoeke, R., Skirving, W., Marra, J., Reyns, J., Aucan, J., et al., 2020. Steps to develop early warning systems and future scenarios of storm wave-driven flooding along coral reef-lined coasts. Front. Mar. Sci. 7, 199.
Zhang, X., 2022. Field observations of infragravity waves off the Dutch coast. MSc Thesis, Delft Univ. Technol..
Zhang, Q., Toorman, E.A., Monbaliu, J., 2020. Shoaling of bound infragravity waves on plane slopes for bichromatic wave conditions. Coast. Eng. 158, 103684.
Zheng, Z., Ma, X., Ma, Y., Huang, X., Dong, G., 2021. Modeling of coastal infragravity waves using the spectral model WAVEWATCH III. Coast. Eng. 170, 104016.
Zijlema, M., Stelling, G., Smit, P., 2011. SWASH: An operational public domain code for simulating wave fields and rapidly varied flows in coastal waters. Coast. Eng. 58 (10), 992–1012.